

# **EXPERIMENTAL INVESTIGATION OF GDI INJECTORS**

**A Thesis Submitted to  
the Graduate School of Engineering and Sciences of  
İzmir Institute of Technology  
in Partial Fulfillment of the Requirements for the Degree of  
MASTER OF SCIENCE  
in Mechanical Engineering**

**by  
Fakhry Abuzahra**

**November 2015  
Izmir**

We approve the thesis of **Fakhry Abuzahra**

Examining Committee Members:

---

**Assist. Prof. Dr. Ünver ÖZKOL**

Department of Mechanical Engineering, Izmir Institute of Technology

---

**Assist. Prof. Dr. Turhan ÇOBAN**

Department of Mechanical Engineering, Ege University

---

**Assist. Prof. Dr. Alvaro DIEZ**

Department of Mechanical Engineering, Izmir Institute of Technology

**24 November 2015**

---

**Assist. Prof. Dr. Alvaro DIEZ**

Department of Mechanical Engineering  
Izmir Institute of Technology

---

**Prof. Dr. Metin TANOĞLU**

Head of the Department of  
Mechanical Engineering

---

**Prof. Dr. Bilge KARAÇALI**

Dean of the Graduate School of  
Engineering and Sciences

## **ACKNOWLEDGMENTS**

I would never be able to accomplish the thesis work without the guidance of my supervisor, co-supervisor, family, friends and my great lab colleagues.

I would like to express my sincere gratitude to my supervisor Assist.Prof. DIEZ Alvaro who was teaching, guiding, explaining and facilitating this long journey and without him I could not be able to show up this thesis. I would like to mention the Department of Industrial Engineering at the University of Perugia, Italy who facilitates my period of experiments at the Spray Labs under the direct supervision of Prof. POSTRIOTI Lucio who offered the facilities to complete the work as well as guided me step by step until the last rock of the thesis. Eng. BOSSI Maurizio , Eng. CAVACCHI Andrea and Eng. OTTOBRE Fabrizio were my lab colleagues to whom I am sending my great thanks and wishes for a successful life since they were teaching, guiding and helping me from the first day of arrival.

I would like to thank the Scientific and Technological Research Council of Turkey (TUBITAK) who supported my thesis financially for a year in both Turkey and Italy as well.

At the end, I am willing to thank my family and specially my eldest brother Inst. Alaa for his inspiring advice, and my great Wife Eng. Dana who offered me a quite atmosphere and was brave enough to withstand the whole period I was away from her.

# ABSTRACT

## EXPERIMENTAL INVESTIGATION OF GDI INJECTORS

Among the challenges in the internal combustion - spark ignition Gasoline Direct Injection (GDI) engines stayed under spotlight for its ability to be developed in terms of fuel conversion efficiency and emission contaminants. Spray analysis is of great importance for the combustion operation and it is a prerequisite for improving the mixing capabilities of the air/fuel mixture. Momentum flux measurement technique is one of the most interesting approaches that aims to study the spray structure which can be a complement for high-speed imaging and Phase Doppler Anemometry (PDA) analysis.

In the present study, two GDI single-hole research injectors, Magneti Marelli with Length to Diameter parameter ( $L/D$ )=1, 3 are investigated by means of momentum flux, global and local, under both low and high temperatures. The flash-boiling phenomenon is triggered when static pressure is below fuel saturation pressure at the same temperature which drastically affects the spray structure in terms of decrement in the penetration rate accompanied with an enlargement in the cone angle. N-heptane is used as a fuel under a temperature range 30 – 120 °C, vessel ambient pressure range 40 – 303 KPa, energizing time 1500 – 3000  $\mu$  distance for the global momentum 5 – 40 mm and two horizontal planes for local momentum flux 10, 30 mm. Results of high-speed imaging were integrated in terms of cone angle and penetration rate. Furthermore, the results of this study can verify the Computational Fluid Dynamic (CFD) numerical analysis and provide wealthy understanding of the spray evolution.

# ÖZET

## DIREK BENZİN ENJEKTÖLERİNİN DENEYSEL ARAŞTIRILMASI

Günümüzde, yanma motorun optimizasyonunda Benzin Direk Enjeksiyon teknoloji önemli alanlardan biri olmuştur. Günden güne emisyon mevzuatları daha daralmaktadır. Bu motor tasarımcılarının için araştırma yapmalarına engel olmaktadır. İçten yanma motorlarının araştırılması sırasında sprej şekilleri ve analizleri dikkate alınması gerekmektedir. Sprej analizindeki momentum akışının ölçüleri oldukça önemli bir teknik olarak sayılmaktadır. Yüksek hızlı görüntüleme, sprej momentum akışının ölçülerine yardımcı olarak kullanılacaktır.

Mevcut çalışmada, araştırma olarak iki tek-delikli GDI Magneti Marelli markalı enjektör kullanılmaktadır. Bu enjektörler için momentum akışı ölçüleri hem global hem de mekansal olarak, yüksek ve düşük sıcaklıklarda yapılmıştır. Adı geçen flaş-kaynama fenomen statik basınç akışkanın basıncından daha düşüktür ve ikisinde aynı sıcaklıkta tetiklenmektedir. Akışkan olarak 30 – 120 °C sıcaklığındaki N-Heptane kullanmıştır. Basınç olarak yanma odasının basıncı olan 40 – 303 *KPa* arası kullanmıştır. Flaş-kaynama'da sprejin penetrasyonu oranının azaltılmasını ve sprejin konik açısı genişletilmesini etkilemektedir. Momentum akışının sonuçları yüksek-hızlı görüntüleme ile birlikte numerik sonuçlarına doğrulamaktadır.

# TABLE OF CONTENTS

LIST OF FIGURES .....	viii
LIST OF TABLES .....	x
LIST OF ABBREVIATIONS .....	xi
CHAPTER 1. INTRODUCTION .....	1
CHAPTER 2. LITERATURE SURVEY .....	3
2.1. Introduction to Gasoline Direct Injection GDI Engines .....	3
2.1.1. Brief commercial history .....	3
2.1.2. GDI Features .....	3
2.1.3. Challenges and Proposed Solutions .....	5
2.1.3.1. Increasing Compression Ratio .....	5
2.1.3.2. Emission Legislation .....	6
2.1.3.3. Fuel Consumption .....	7
2.2. Spray Characteristics in GDI .....	7
2.2.1. Introduction.....	8
2.2.2. Atomization .....	9
2.2.2.1. Breakup Regimes .....	9
2.2.2.2. Breakup Model .....	10
2.2.3. Spray Cone Angle .....	13
2.2.4. Spray Momentum Flux .....	14
CHAPTER 3. EXPERIMENTAL SETUP .....	20
3.1. Introduction.....	20
3.2. Experimental Setup .....	20
3.2.1. Schematic Diagram .....	20
3.2.2. Momentum Test Rig .....	20
3.2.2.1. Current Profile, Injector Control .....	21
3.2.2.2. Spatial Momentum Flux-Cone .....	22
3.2.2.3. Target.....	22

3.2.2.4. Force Sensor .....	24
3.2.2.5. High-Speed Imaging Technique .....	24
3.2.3. Spray Penetration.....	25
3.2.4. Cone Angle .....	27
3.3. Experimental Procedure.....	27
3.4. Experimental Strategies .....	29
CHAPTER 4. RESULTS .....	31
4.1. Spray Momentum Flux.....	31
4.1.1. Global Momentum Test .....	31
4.1.2. Local Momentum Test .....	51
4.1.3. Comparison Between Local and Global Momentum .....	55
4.2. Penetration Rate .....	57
4.3. Spray Cone Angle .....	58
CHAPTER 5. CONCLUSION .....	64
REFERENCES .....	66

# LIST OF FIGURES

<u>Figure</u>	<u>Page</u>
Figure 2.1. Direct injection principle. Source: (Carsten, 2006) .....	4
Figure 2.2. Wall-guided and spray-guided. Source: (Zhao, 2010) .....	8
Figure 2.3. Schematic diagram for boosted-aspirated Vs Naturally-aspirated engine. Source: (Zhao, 2010) .....	8
Figure 2.4. Breakup regimes. Source: (RD and FV, 1986) .....	10
Figure 2.5. Schematic diagram of the jet breakup curve. Source: (Leroux et al., 1996) .....	11
Figure 2.6. Stability curve of a cylindrical jet flow behavior. Source: (Leroux et al., 1996) .....	13
Figure 2.7. Schematic of cone angle. Source: (Desantes et al., 2006) .....	14
Figure 2.8. Principle of momentum flux measurement. Source: (Payri et al., 2005) .	15
Figure 2.9. Scheme of control volume for momentum flux analysis. Source: (Postrinoti et al., 2011) .....	15
Figure 2.10. Relation between discharge coefficient and cavitation number. Source: (Payri et al., 2005) .....	17
Figure 3.1. Schematic diagram for the momentum flux measurement technique. ....	20
Figure 3.2. Momentum flux vessel. ....	21
Figure 3.3. Momentum flux fixture and moving system. ....	22
Figure 3.4. The values of the current profile. ....	23
Figure 3.5. Spatial momentum test cone-fixture. ....	23
Figure 3.6. Different target shapes. ....	24
Figure 3.7. Kistler force sensor. ....	24
Figure 3.8. Centering for local test utilizing high speed imaging. ....	25
Figure 3.9. Centering for global test utilizing high-speed imaging-video technique. ....	26
Figure 3.10. Zeroing program-interface. ....	26
Figure 3.11. feedback control system interface. ....	27
Figure 3.12. Calculating cone angle utilizing spatial momentum results. ....	28
Figure 4.1. Effect of vessel pressure on the detected force on IHP-279, IHP-293 injectors. ....	32
Figure 4.2. Comparison among IHP-279, IHP-293 injectors under flash-boiling effect. ....	34



Figure 4.3. The effect of injection pressure over different vessel pressure at non flash-boiling condition. ....	36
Figure 4.4. The effect of injection pressure over different vessel pressure at flash-boiling condition. ....	38
Figure 4.5. The effect of energizing time at Tf 30 C over different vessel pressures. ....	39
Figure 4.6. Effect of energizing time at 90 C fuel temperature. ....	40
Figure 4.7. Comparison among the height distance Z for IHP-293-P100,ET1500,Tf30 42	
Figure 4.8. Comparison among the height distance Z for IHP-293-P100,ET1500,Tf120 44	
Figure 4.9. Effect of fuel temperature over different vessel pressure at distance Z=10 mm. ....	46
Figure 4.10. Magnification of the effect of temperature on the spray over different vessel pressure at distance Z=10 mm. ....	47
Figure 4.11. Effect of temperature on the spray over different vessel pressure at distance Z=30 mm. ....	49
Figure 4.12. Magnified of the effect of temperature on the spray over different vessel pressure at distance Z=30 mm. ....	50
Figure 4.13. Global momentum flux-integrated measurements. ....	51
Figure 4.14. Local momentum flux results, IHP-293 ....	53
Figure 4.15. Effect of vessel pressure on the local momentum flux. ....	56
Figure 4.16. Effect of vessel pressure on the penetration rate. ....	59
Figure 4.17. Effect of fuel temperature on the penetration rate. ....	60
Figure 4.18. Comparison of penetration rate measured from momentum VS imag- ing; blue refers to momentum, and dark red refers to high-speed imag- ing, imaging results are integrated from (Bosi, 2014). ....	61
Figure 4.19. Cone angle measurement concept utilizing local momentum flux. ....	62
Figure 4.20. High speed imaging for different experimental conditions for IHP-293 injector. Source: (Postrioti et al., 2015) ....	63

# LIST OF TABLES

<b><u>Table</u></b>	<b><u>Page</u></b>
Table 2.1. Aftertreatment-systems properties .....	7
Table 2.2. Regime types with its corresponding Weber number value. ....	12
Table 2.3. clarification for figure 2.6 .....	13
Table 3.1. The working condition with the corresponding AtSPR-values. Source: (Xu et al., 2013) .....	29
Table 3.2. Ranges of ASPR for flash-boiling effect. ....	29
Table 3.3. Injectors specifications. ....	30
Table 3.4. Generic test plan for different pressure, temperature and energizing time conditions. ....	30
Table 4.1. Global momentum flux integral form with the related operating condi- tions. ....	52
Table 4.2. Comparison between the integrated local momentum flux and the global one. ....	57

## LIST OF ABBREVIATIONS

<b>GDI</b>	Gasoline Direct Injection
<b>CFD</b>	Computational Fluid Dynamic
<b>L/D</b>	Length to Diameter parameter
<b>DI</b>	Direct Injection
<b>FSI</b>	Fuel Stratified Injection
<b>TSI</b>	Turbo Stratified Injection
<b>PFI</b>	Port Fuel Injection
<b>LBDI</b>	Lean Boosted Direct Injection
<b>EGR</b>	Exhaust Gas Recirculation
<b>CR</b>	Compression Ratio
<b>BMEP</b>	Break Mean Effective Pressure
<b>OBD</b>	On-Board Diagnostic
<b>NEDC</b>	New European De-pollution Cycle
<b>We</b>	Weber number
<b>AtSPR</b>	Air to Saturation Pressure Ratio
<b>DOE</b>	Design of Experiment
<b>N/V</b>	Newton per Volt
<b>PDA</b>	Phase Doppler Anemometry
<b>HC</b>	Hydrocarbons
<b>NI</b>	National Instrument
<b>ET</b>	Energizing Time
$T_f$	Fuel Temperature

$T_p$  Tip Temperature

$P_v$  Vessel Pressure

$P_{inj}$  Injection Pressure

**Z** Sensor Distance

# CHAPTER 1

## INTRODUCTION

Recently, awareness of exhaust gases, in particular those come from vehicles, has dramatically increased. Therefore, the legislation of emission whether for  $CO_2$  or  $NO_x$ , ...etc , is becoming tighter to strict it to a specific value (Zhao, 2010), which has been the incentive for car factories and research centers to pay more attention to GDI engines. The advantages of those engines are of great importance to change trends towards them; the downsizing with turbo-charging and/or super-charging technologies accompanied with GDI has opened a wide gate to improve the thermodynamic efficiency and therefore lessen the fuel consumption.

GDI can resist knocking in peculiar operation conditions such as part-load due to its direct fuel injection principle accompanied with different spray spreading-out techniques such as spray-guided and wall-guided. In order to achieve the knock resistance it is important to utilize stratified charge concept, in which the air/fuel ratio is greater near to the spark plug whereas it gradually becomes less towards the cylinder walls, (Zhao, 2010). Going down in the hierarchy, the spray analysis is basically the basis of combustion in the internal combustion engine. However, different techniques have been proposed in order to better understand the spray both internal structure and general external-shape as well. Controlling the spray mixing capabilities is mandatory along with the GDI analysis to predict the interactions between spray and the surrounding air.

However, among the experimental approaches, momentum flux measurements with both global and spatial forms are of primary importance for providing a quantitative analysis for the spray structure, which is more convenient than the traditional techniques such as Doppler analysis. Furthermore, the momentum flux measurement mandates several constraints such as steady state process and the orthogonality between the impinged-spray and the sensor plate. However, the steady state condition is achieved by increasing the energizing time which makes the experiment far from the engine-like working condition. To cope with that problem, A special care is payed to the experimental setup. High speed imaging is of primary importance for comprehending spray structure in terms of penetration rate and cone angle as well. However, the high speed imaging technique is

integrated in this work, hence, it is used for the purpose of alignment the spray jet with the sensor-target. A small portion of the jet was studied under the name of spatial momentum flux which, aimed to analyze the internal spray structure.

The first chapter consists of a general introduction of the topic follows by the introduction of each chapter.

In the second chapter, the literature survey chapter starts with a brief commercially introduction for GDI engines; mentioning its main features as well as the difficulties facing engine manufactures and how GDI proposes the solution. Later on a deep study of the spray characteristics for GDI is discussed. Lastly, a detailed review for the momentum flux measurement technique and high-speed imaging as well will be presented.

In the third chapter, a general introduction for the experimental setup is presented. Later on, a schematic diagram showing the main steps is presented. After that, the momentum flux measurement technique is presented from both software and hardware aspects, followed by spray cone angle and penetration rate and their importance for spray analysis. The procedure of the experiment is discussed in details, lastly the experimental strategies are explained.

The fourth chapter is the results chapter, in which the results of spray momentum with its global and local types are presented. A comparison among the global and local momentum is held. Later on, the results of penetration rate and spray cone angle are presented and discussed.

In the fifth chapter, a brief conclusion is presented in addition to some possible future trends.

## CHAPTER 2

### LITERATURE SURVEY

#### 2.1. Introduction to Gasoline Direct Injection GDI Engines

##### 2.1.1. Brief commercial history

GDI has been used commercially for two decades. In 1996 Mitsubishi produced a modern GDI engine with 1.8 L straight-4 Galant/Lengum motors and in 1997 Mitsubishi Carisma was presented to the European market (Iwamoto et al., 1997). Later on, Mitsubishi and Toyota spread out their cars with GDI technology to both Japan and Europe to reach a million GDI-based cars by 2001. From a technical point of view, these kind of cars were designed to work in a stratified-charge spark-ignition combustion mode at part load with speed ranges from low to high, and a homogeneous charge at high-load high-speed operation condition. Because of the introduction of tighter emission legislation, after-treatment of stratified lean-burn operations became more expensive and less efficient for lean-burn  $NO_x$  emission, though after 2001 DI was used only in a homogeneous charge mode. To overcome this problem, Toyota used a combination of port injection and in-cylinder direct injection in order to provide smooth operation in all charge-modes.

VW and Audi groups have used Direct Injection (DI) frequently under the trade mark of Fuel Stratified Injection (FSI). They aimed to produce smaller engines with higher output power, so they used the two-stage Turbo Stratified Injection (TSI) 1.4 L using mechanical turbocharger and supercharger and they gained 90 Kw/l power density. However, in 2007 BMW produced its high-precision direct injection 3.0 L engine (Schwarz et al., 2006), and thus it both improved the overall efficiency and widened the time range of the lean-burn. Nowadays, GDI engines are being spread out rapidly among many companies all over the world. However, better fuel consumption and higher engine efficiency, as well as obeying to the emissions' legislation are incentives for engine makers and developers.

## 2.1.2. GDI Features

GDI engines dictate injecting the fuel directly to the combustion chamber, see figure 2.1, unlikely to Port Fuel Injection (PFI) in which fuel is injected into the intake ports.

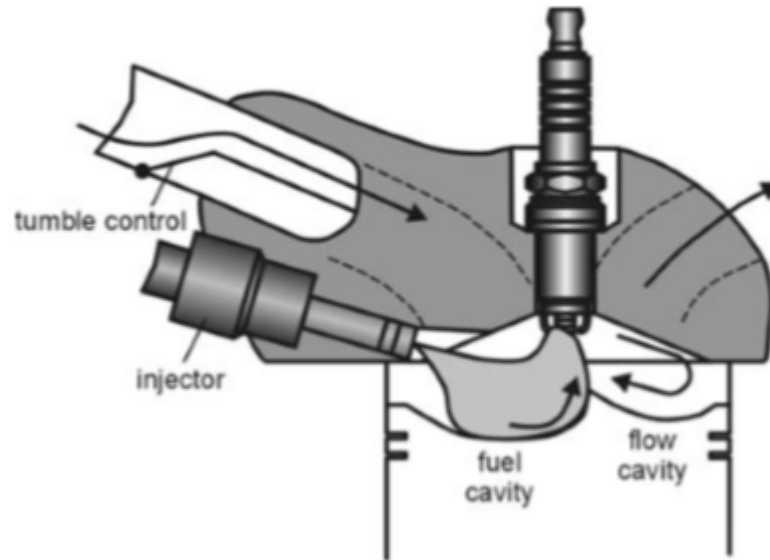


Figure 2.1. Direct injection principle.  
Source: (Carsten, 2006)

When injection takes place, spray evaporates by taking the heat from its surroundings and consequently decreases the in-cylinder temperature, which is called charge cooling effect. Hence, at full load condition the charge cooling effect is well enough to increase the compression ratio by a couple of times far from the knocking combustion limit. Thus using the DI technology increases the limit of knock-resistance at both low and mid-engine-speed conditions (Michael et al., 2005).

The techniques of decreasing the engine size " downsized-engine ", turbo and/or supercharger and throttless operation are technologies that work together interactively to improve fuel consumption issues. Throttle by itself increases mechanical losses. However, working without throttle decreases those losses, which in turn increases the thermal efficiency and respectively decreases fuel consumption.

The working principle of GDI enables the possibility of shutting off the engine during the idle time. It is known that when engine works in the idle time, nearly 10% of the total fuel as an increment is consumed according to the urban driving cycle. Let's



propose a scenario for an urban driving cycle for a PFI and a GDI. In this comparison two points should be carefully taken into account: the energy needed for restarting the engine and the quickness of that. In other word, the engine should be started immediately when the driver decides to drive. However, PFI engine needs several engine-cycles to start, during which it consumes an amount of fuel as if the engine works 5 seconds at idle condition. On the contrary to starting of PFI engines, GDI engine does need neither time nor much fuel, due to the short cranking needed to start the engine. However, for a better stop-auto-start system in both compression-stroke and expansion-stroke, the piston should stop at a proper position to achieve the right balance of air volume. As an example, Mazda has developed a smart system that is able to start the engine within 0.35 second which is estimated to be the half time of an ordinary motor idling stop system (Zhao, 2010).

At higher fuel temperatures, the spray evidences a peculiar behavior especially when static pressure is lower than fluid saturation pressure at the same fluid temperature, which is termed as flash-boiling phenomenon (Xu et al., 2013). Moreover, flash-boiling effect can be beneficial to the GDI engines since it improves the evaporation capabilities and mixing performance. Above all, it results in several modifications among the spray parameters such as shortening in the penetration rate accompanied with a wider flow cone angle, and definitely a better atomization.

### **2.1.3. Challenges and Proposed Solutions**

The challenges could be classified as the following:

#### **2.1.3.1. Increasing Compression Ratio**

The ordinary gasoline engine works with a 10:1 compression ratio, whereas an increment, for example 14:1, significantly reduces fuel consumption, 10% for that example. Increasing Compression Ratio (CR) is hindered by knocking which happens at full load conditions. However, there are several approaches to enlarge knock-resistance limitation. Since knocking is sensitive to the compression temperature of the air/fuel mixture, increasing the octane number can increase the expansion ratio, which is the first approach. Another approach which is expensive and inapplicable, is to vary the compression ra-

tio corresponding to the load, i.e. maximize it at part load and minimize at full load. Nevertheless, there is a possibility to alter the geometric ratio in addition to the actual compression and expansion ratios via retarded or early closing the intake valve; Miller and Atkinson cycles are the examples of that. Above all, high speed power is limited by the high exhaust temperature which may harm the turbocharger parts. In order to apply the aforementioned issues, subsequently, more fuel should be injected, which increases fuel consumption dramatically (Zhao, 2010).

However, there are two technical approaches to overcome knocking: Lean Boosted Direct Injection (LB DI) and Exhaust Gas Recirculation (EGR). Both of them are capable to increase the knock-resistance limit as well as Break Mean Effective Pressure (BMEP). LB DI provides a substantial decrement in the fuel consumption. Despite such a decrement, very lean mixture frequently results in a non-homogeneously distributed high-temperature and high diluted mixture, which increases  $NO_x$  formation (Michael et al., 2005).

### **2.1.3.2. Emission Legislation**

The introduction of GDI under the homogeneous charge is not different from Port Fuel Injection PFI in terms of emission formation. While utilizing stratified charge increases the emission instead of decreasing it, the charge cooling effect in the part load dictates cooling the outer boundary of the charge, and increases the unburned gases in the cylinder. In addition to the liquid within the injected-spray. Moreover, lowering the overall lean-burn as well as the in-cylinder temperature by direct injection, increases Hydrocarbons (HC) by reducing oxidation of the after-burn flame more than that of the homogeneous charge.

There are different technologies to reduce  $NO_x$ . EGR is an effective technology collaborating with some other technologies to achieve the allowance emission rate. Table 2.1 shows the different types of after-treatment technologies with some of their properties.  $NO_x$  trap system needs additional sensors and On-Board Diagnostic (OBD) for durable working. SCR catalyst mandates a separate urea storage and delivery in addition to a closed-loop system on board (Zhao, 2010). Nonetheless, utilizing this type of catalyst decreases the feasibility of GDI to lessen fuel consumption dramatically. Therefore, it can be declared that there is no big improvement whether lean or homogeneous mixture is utilized according to the New European De-pollution Cycle (NEDC), despite that for

lean mixture it is always consumed less gasoline than for the homogeneous one (Michael et al. 2005).

Table 2.1. Aftertreatment-systems properties

<b>Catalyst type</b>	<b>Temperature range (° C)</b>	<b>Conversion efficiency (%)</b>	<b>Compatibility with closed three way-catalyst for cold start</b>	<b>Sensitivity to sulfur content in the gasoline</b>	<b>Need more fuel combustion</b>
<i>D</i> $NO_x$ catalyst/ <b>Lean-<math>NO_x</math></b>	180-300	30-50	No		need
<b><math>NO_x</math> trap/<math>NO_x</math> storage catalyst</b>	200-550	90	yes	low to zero	need

### 2.1.3.3. Fuel Consumption

To have significant fuel consumption reduction, engine downsizing is of great importance. In order to achieve that reduction, the engine is forced to work in its highest efficiency region. The aim of downsized-engine is to decrease the pumping losses, which in turn gains significant fuel consumption reduction; via utilizing lean-burn and allowing the engine to work in a wider throttle operation. There is a limitation for the lean-burn represented in the air/fuel ratio up to 20:1 which can be increased up to 100:1 by adopting stratified charge (Zhao, 2010). Acquiring this type of charge dictates adopting mainly two basic approaches; wall-guided and spray-guided, for more illustration see Figure 2.2.

In the spark ignition gasoline engine, the maximum boosted pressure is restricted by knocking, (Figure 2.3. Therefore, utilizing DI engine gives the ability to produce downsized boosted-engine by means of charge cooling effect. However, downsized boosted-engine and direct injection are working interactively in a way to reduce fuel consumption.

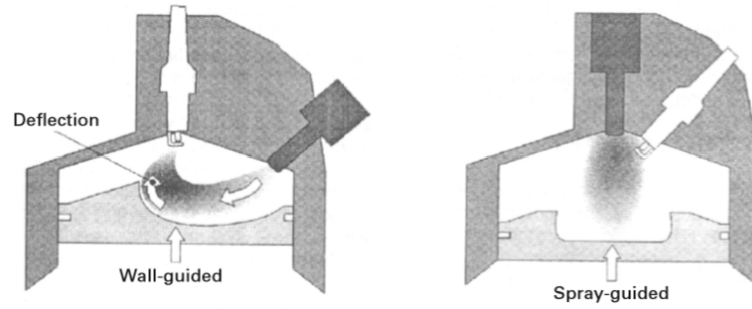


Figure 2.2. Wall-guided and spray-guided.

Source: (Zhao, 2010)

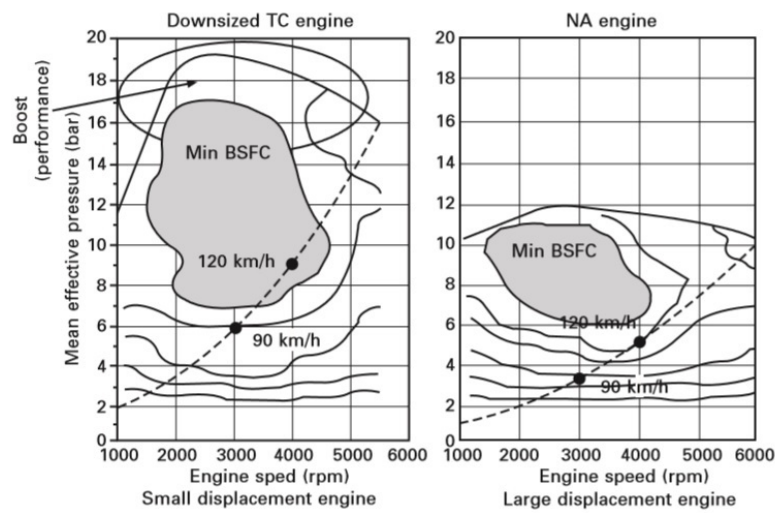


Figure 2.3. Schematic diagram for boosted-aspirated Vs Naturally-aspirated engine.

Source: (Zhao, 2010)

## 2.2. Spray Characteristics in GDI

### 2.2.1. Introduction

Recently, obeying to the emission legislation and attaining higher efficiency as well as better fuel consumption have been the incentives for engine manufacturers. For that purpose comprehending air/fuel mixture is obligatory. However, for a better understanding it can be divided into several parts such as air entrainment characteristics, fuel charge and exhaust emissions.

For GDI engines several charge patterns such as homogeneous charge are proposed to achieve some purposes, some of which is the decreasing emission rate. However, having such a pattern of charge needs specific spray characteristics, which are normally analyzed at all levels starting from atomization and ending up with breakup-vapor. In the next sections, a brief theoretical review about atomization regimes and spray characteristics as well as some proposed techniques for measuring them are presented.

## **2.2.2. Atomization**

Atomization is an essential part of the optimization process for direct injection engines, hence, variety ways can be followed to well-understand it. In the next sections, a numerical-theoretical-background for both regimes as well as a proposed model for breakup are presented.

### **2.2.2.1. Breakup Regimes**

Spray emanated from the nozzle starts by primary breakup through transforming into ligaments, sheets and drops. Then, it is followed by a secondary breakup where larger droplets become smaller, by going downstream the nozzle. However, many postulations for simulating, predicting several spray parameters have been done. Despite that, there is still an ambiguity in distinguishing those breakup under different circumstances.

Breakup can be divided into four regimes according to the combination of liquid inertia, surface tension and aerodynamic forces that act on the jet (RD and FV, 1986). Figure 2.4 represents the four regimes, from a-d respectively; Rayleigh, first wind-induced, second wind-induced and the atomization regimes.

The droplets' sizes are of the same order of the nozzle diameter in both Rayleigh and first wind-induced, whereas in second wind-induced as well as atomization regimes are much smaller. Breakup commences just on the nozzle exit in both second wind-induced and atomization, because they have smaller drops. While it happens several diameters downstream the nozzle in the other regimes.

At each regime type there is an unbroken liquid core, and hence, it is the basis for another categorization according to its length  $L$  which is a function of the jet velocity  $U$  (Leroux et al., 1996), (Figure 2.5. However, breakup length over curve (a) is linearly

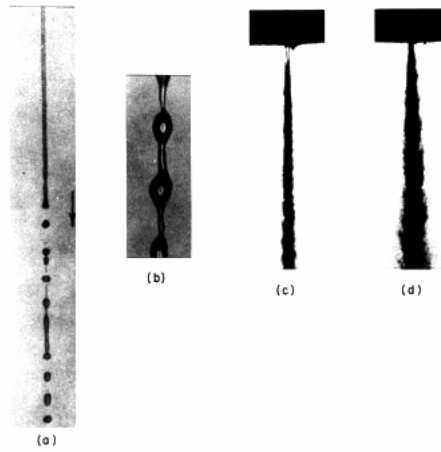


Figure 2.4. Breakup regimes.  
Source: (RD and FV, 1986)

related to the jet velocity before reaching the peak then it is decreasing over the curve (b). The concert between the first and the second regimes is predicted utilizing stability theories (Sterling and Sleicher, 1975).

### 2.2.2.2. Breakup Model

According to the linear stability theories, the perturbation (of the liquid surface emanates from a circular jet) can be governed by a Fourier component of the form:

$$\eta = \eta_0 \exp(\omega t + iKx) \quad (2.1)$$

where ( $\eta$ ) is a function of distance and time and resembles the displacement of the liquid surface; ( $\eta_0$ ) is the initial perturbation; ( $K$ ) is the wave number; ( $\omega$ ) is the complex frequency.

The dispersion equation over the maximum growth rate ( $\omega_r = \Omega$ ) with its corresponding wave length ( $\lambda = \Lambda$ ) is numerically solved in equations 2.2 & 2.3 (Reitz, 1987).

$$\frac{\Lambda}{a} = 9.02 \frac{(1 + 0.45 Z^{0.5})(1 + 0.4 T^{0.7})}{(1 + 0.87 We_2^{1.67})^{0.6}} \quad (2.2)$$

$$\Omega \left( \frac{\rho_1 a^3}{\sigma} \right)^{0.5} = \frac{0.34 + 0.38 We_2^{1.5}}{(1 + Z)(1 + 1.4 T^{0.6})} \quad (2.3)$$

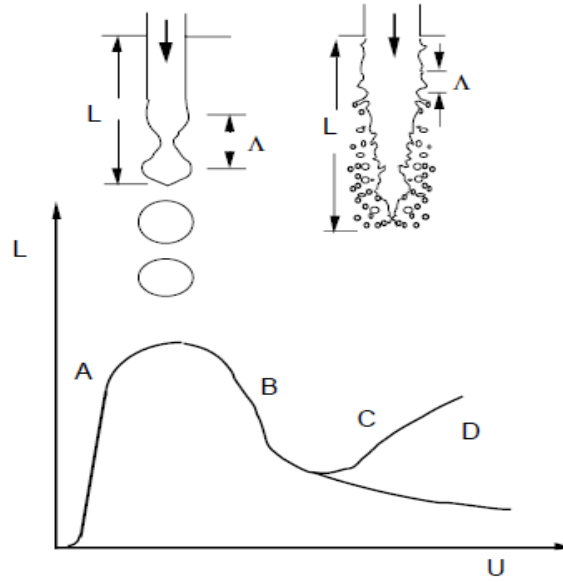


Figure 2.5. Schematic diagram of the jet breakup curve.  
Source: (Leroux et al., 1996)

where Ohnesorge number,  $Z = \frac{\sqrt{We_1}}{Re_1}$ ; Taylor parameter,  $T = Z\sqrt{We_2}$ ; Weber number,  $We_1 = \frac{\rho_1 U^2 a}{\sigma}$ ; Reynolds number,  $Re_1 = \frac{Ua}{\nu_1}$ ;  $a$  is the radius of the jet;  $U$  is the relative velocity between the jet and gas; 1&2 subscriptions are used for liquid and gas properties, respectively. However, at small Weber number ( $We$ ) breakup starts when the dominant wave is of the same radius of the jet, hence the breakup length is given by equation 2.4 (Lin and Reitz, 1998).

$$L = U\tau = U/\Omega \ln(a/\eta_0) \quad (2.4)$$

where  $\tau$  is the breaking time given by:  $a = \eta_0 \exp(\Omega\tau)$ .

According to the (Sterling and Sleicher, 1975) theory, the disagreement in the curves c,d owes to the nozzle internal flow pattern changes due to the cavitation and separation phenomena (Leroux et al., 1996), (Lin and Reitz, 1998).

It is worth to mention that the condition  $L = U\tau$  in equation 2.4 is acceptable and well-predictable for the breakup length providing that the gas density is significant. In other words, capillary pinching is the predominant of the breakup mechanism. However, for high jet-velocity, capillary pinching is not the breakup-responsible anymore. Instead, the unstable growth of the short-wavelength surface wave will be the responsible for the breakup (Lin and Reitz, 1998). However, achieving details in the high jet-velocity condi-

tion is hindered by the spray dense at the injector tip.

Before (Leroux et al., 1996), (Reitz and Bracco, 1982) have stated that droplets strip from the unbroken liquid core near to nozzle exit due to the aerodynamic forces at the liquid/gas interface. the unbroken core-length is given by equation 2.5, (Taylor, 1940).

$$L/a = B(\rho_1/\rho_2)^{1/2}/f(T) \quad (2.5)$$

where Taylor parameter,  $T = (\rho_1/\rho_2)(Re_1/We_1)^2$ ; The function  $f(T) = \frac{\sqrt{3}}{6 [1-\exp(-10T)]}$  approximated from Taylor's numerical results (Dan et al., 1997).

The onset of the breakup regimes has been reviewed by (Chigier and Reitz, 1996). (Ranz, 1956) declared that the onset of the breakup for the first wind-induced regime is no longer governed only by ( $We_L > 8$ ) condition, however, the criterion of ( $We_g \equiv \frac{\rho_2 U^2 (2a)}{\sigma} < 0.4$ ) which refers to the point where the inertia force of the surrounding gas is roughly-estimated by 10% of the inertia of the surface tension. However, (Sterling and Sleicher, 1975) postulate that maximum jet breakup length occurs when ( $We_L = 1.2 + 3.41 Z^{0.9}$ ). Thus, relation 2.6 fits properly for Rayleigh breakup regime.

$$We_L > 8 \quad \text{and} \quad We_g < 0.4 \quad \text{or} \quad 1.2 + 3.41 Z_1^{0.9} \quad (2.6)$$

Among the inertia and surface tension balance argument, (Ranz, 1956) bounded the first wind-induced using the value of ( $We = 13$ ), where gas inertia is of the same order of magnitude with the surface tension force at that condition. Therefore,  $We = 13$  is the onset for the second wind-induced breakup regime; as the value of  $We$  increases, it points to the end of forces' balance and the gas becomes the dominant power. However, (Miesse, 1955) postulated the start of the atomization breakup-regime to be at ( $We_g > 40.3$ ). Table 2.2 is a brief summery for the proposed breakup-regime-bounding criteria, providing that effects of the nozzle internal flow are excluded from that criteria.

Table 2.2. Regime types with its corresponding Weber number value.

Regime type	bounded creterion
Rayleigh	$We_L > 8 \quad \text{and} \quad We_g < 0.4 \quad \text{or} \quad 1.2 + 3.41 Z_1^{0.9}$
First wind-induced	$1.2 + 3.41 Z_1^{0.9} < We_g < 13$
Second wind-induced	$13 < We_g < 40.3$
Atomization	$We_g > 40.3$

For more clarification, Figure 2.6 with the corresponding values in Table 2.3 illustrate an example for the aforementioned regimes.



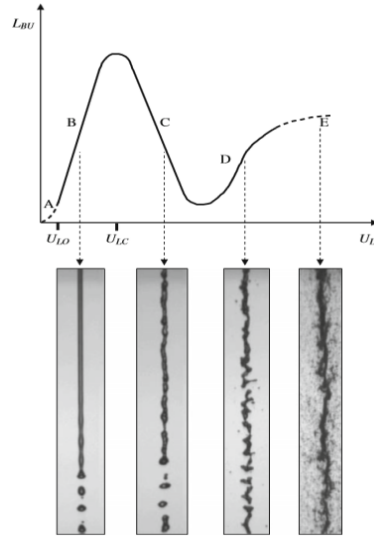


Figure 2.6. Stability curve of a cylindrical jet flow behavior.  
Source: (Leroux et al., 1996)

Table 2.3. clarification for figure 2.6

Region	Regime-type	$Re_L$	$We_G$
B	Rayleigh	790	0.06
C	First wind-induced	5500	2.7
D	Second wind-induced	16500	24
E	Atomization	28000	70

Taking the internal nozzle flow effects into account, the onset of the atomization is triggered when Condition 2.7 is achieved.

$$\frac{\rho_2}{\rho_1} > K f(T)^{-2} \quad (2.7)$$

where  $K$  is a parameter found experimentally to be equal to

$$K = \frac{0.53[3 + (l/2a)]^{1/2} - 1.15}{744}$$

Parameter ( $K$ ) accounts for the initial disturbances such as cavitation, flow separation and turbulence as well as the effect of liquid viscosity (Lin and Reitz, 1998).

### 2.2.3. Spray Cone Angle

Cone angle measurement assists for comprehending spray structure as well as being an indication for the air/fuel mixing quality. It can be defined as the angle bounded between the edges of the spray and at 0.6 of the penetration rate, Figure 2.7.

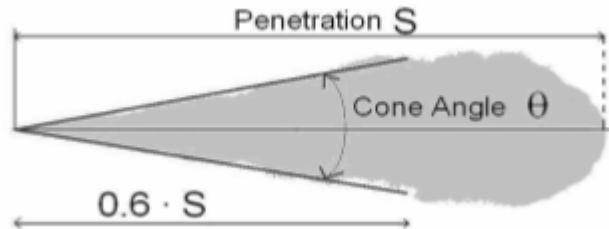


Figure 2.7. Schematic of cone angle.  
Source: (Desantes et al., 2006)

However, cone angle can be measured using high speed imaging techniques either imaging or a short-video. In fact, the introduction of spatial momentum technique is not only allotted only for momentum flux analysis, but also for measuring the cone angle as mentioned in spray momentum flux section.

### 2.2.4. Spray Momentum Flux

Spray momentum flux measurement is one of the important tools for comprehending the spray structure in addition to study the effect of nozzle diameter on the spray formation. Further assisting-measurements can be performed to calculate for different phenomena such as cavitation. Simply, the lower momentum flux has the higher evaporation rate and respectively higher air/fuel mixing potential.

Figure 2.8 illustrates the principle of momentum flux measurement which is constrained by the conservation of momentum law (Payri et al., 2005). However, the force of a spray emanates from a circular nozzle perpendicularly on a target of force sensor equates the momentum flux; providing a steady-state condition and a large-enough target to acquire all spray in a way that all the impinged-spray is deflected perpendicularly to the axis of motion (Postrioti et al., 2011).

The physical background behind spray momentum flux measurement is illustrated

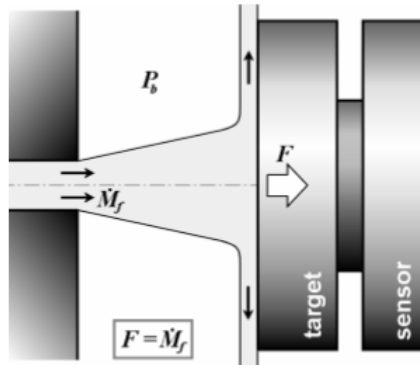


Figure 2.8. Principle of momentum flux measurement.  
Source: (Payri et al., 2005)

in Figure 2.9. The conservation of momentum for such a system can be shown in Equation 2.8. For steady state condition, the first term can be canceled. Additional to that, gravity as well as tangential stresses respect to the target are neglected, therefore,  $F = \dot{M}$ .

$$F = \frac{\partial}{\partial t} \iiint_v \rho \vec{v} dV + \iint_s \rho \vec{v} (\vec{v} \cdot \vec{n}) dS \quad (2.8)$$



Figure 2.9. Scheme of control volume for momentum flux analysis.  
Source: (Postrioti et al., 2011)

However, special care should be taken to achieve the steady state. Energizing time should be long enough in addition to consider only the mean value of the spray momentum flux by omitting the onset and the closing response values.

Measuring the mass flow rate, which in turn, makes use of the momentum flux measurements to study the discharge capability and liquid-vapor interactions together with several hypothesis; uniform flow velocity ( $v_{eff}$ ), an effective area separated between the two phases ( $A_{eff}$ ), keeping in mind that there is no contribution for vapor phase is taken into account in the momentum flux measurement (Postrioti et al., 2011). Equations 2.9 and 2.10 illustrate the effective mass flow rate and the momentum flux, respectively.

$$\dot{m} = \rho_l v_{eff} A_{eff} \quad (2.9)$$

$$\dot{M} = \rho_l v_{eff}^2 A_{eff} \quad (2.10)$$

The theoretical velocity is in Equation 2.11 which is derived by applying Bernoulli's equation between the inlet and outlet of the nozzle under the assumption of null inlet velocity.

$$u_{th} = \sqrt{\frac{2\delta P}{\rho_l}} \quad (2.11)$$

Effective velocity can be calculated using Equation 2.10 divided by Equation 2.9 as in Equation 2.12.

$$v_{eff} = \frac{\dot{M}}{\dot{m}} \quad (2.12)$$

A velocity reduction factor can be established as in Equation 2.13.

$$C_v = \frac{v_{eff}}{v_{th}} \quad (2.13)$$

A theoretical value for the area ( $A_{th}$ ) can be assumed, therefore, area reduction factor ( $C_a$ ) can be seen in equation 2.14

$$C_a = \frac{A_{eff}}{A_{th}} \quad (2.14)$$

However, area reduction factor ( $C_a$ ) together with velocity reduction factor ( $C_v$ ) can form another non-dimensional parameter called discharge coefficient ( $C_d$ ), (Equation 2.15).

$$C_d = C_v C_a \quad (2.15)$$

According to the first theoretical cavitation-predictable model, based on Figure 2.10 (Nurick, 1976), at an arbitrary section ( $c$ ) there is a reduction area ( $C_c$ ).

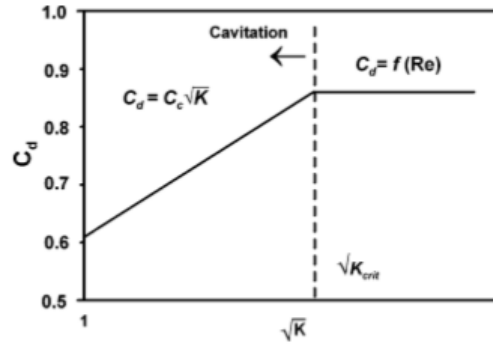


Figure 2.10. Relation between discharge coefficient and cavitation number.  
Source: (Payri et al., 2005)

By applying Bernoulli's equation between a point called ( $i$ ) located upstream and the arbitrary point ( $c$ ), the discharge coefficient ( $C_d$ ) can be calculated as in Equation 2.16. The value of the under-root is defined as the cavitation number ( $K$ ), (Nurick, 1976).

$$C_d = C_c \sqrt{\frac{P_i - P_v}{P_i - P_b}} \quad (2.16)$$

The momentum flux measurement technique has been utilized in several fields. (Desantes et al., 2003) utilized momentum flux accompanied with mass flow rate to study the cavitations effects which may appear at the nozzle holes of the Diesel injector. In that work, they discussed the effect of cavitations on the momentum flux and the outlet velocity. Furthermore, momentum flux analysis has been utilized to predict the penetration rate for Diesel spray, (Desantes et al., 2006). They postulated a model to predict the penetration rate via dividing the momentum flux into packets in which the ones at the top of the spray are leading by their momentum. Those packets follow a theoretical bases in which momentum flux, density and time are related together. High-speed imaging was done as a reference, then a good-agreement, in general, has been achieved between the penetration rate measured by momentum flux and those from the model at a respectively low injection

pressure values, for example 300 bar,  $40\text{kg}/\text{m}^3$ , as well as for a high injection pressure, for example 800 bar.

Later on, (Postrioti et al., 2009) distinguished experimentally and numerically the spray evolution for a Diesel injector, utilizing the global momentum flux measurement. However, the experimental data was used to verify the numerical models. As a working condition; ambient temperature with high back-pressure for the momentum flux measurement was used. High-speed imaging was used as assisting tool for a better internal spray-comprehension.

Momentum flux, in addition to mass flow rate measurements, enable the calculation of the mean velocity at the nozzle outlet as well as the velocity reduction coefficient that appears by cavitation, (Postrioti and Battistoni, 2010). The global momentum flux was accomplished at different elevations with different back-pressure values. For this study, the aim was to analyze the spray via momentum flux technique in transient events, i.e. engine-like, which is normally far enough from the steady state condition which can be beneficial for triggering the shot-to-shot non-uniformity of the spray in some working condition, such as low-load operating condition. The experimental data were used to validate the CFD numerical model. An optimization was done and resulted in a better configuration. However, it is postulated that a dependable estimation for the momentum flux can be achieved in the unsteady flow condition maintaining a suitable target size, i.e. corresponding to the spray size.

Similarly to the Diesel momentum flux analysis, (Postrioti et al., 2012) applied a full analysis on a 3-hole GDI injector in sense of momentum flux, PDA and high-speed imaging to study the internal spray structure and the external spray shape as well. For the three injection pressure values, global momentum was accomplished for height (10-50 mm), 5 mm steps; local momentum (as will be discussed in the following paragraph) at 20 mm plane distance at ambient fuel temperature. Different target diameters were used and distinguished. The difference appeared at a respectively big distance, for example 20 mm, as a more sensitivity to the pressure acting on it. In general, the target should acquire the whole spray, but nevertheless it should not be too much larger than it, because the sensor will trigger the effect of the pressure on the top of the target. The main object in that study was to analyze the spray evolution in terms of cone angle and penetration rate, droplet velocity and distribution as well as size in the time-history maintaining the fuel temperature in the ambient value.

There are two types of momentum flux analysis: global momentum and spatial momentum, which have been verified both experimentally and numerically (Postrioti

et al., 2009), (Postrioti et al., 2011). While global momentum flux technique provides a great insight on the internal design of the nozzle, local momentum flux technique gives information about the quality of the spray structure as well as being a reference for the CFD simulation. Moreover, results of spatial momentum can be useful for comprehending the contribution of several streams inside the jet, which is not attainable by global momentum flux measurements. Additional to that cone angle can be predicted by analyzing the spatial results. During analysis a pre-specified percent of the mean measured-momentum will be taken into account and the furthest measured-stream line that has the acceptable percent of momentum will be the boundary streamline, and hence, the distance from the center of spray will be the leg length of the angle-like for the cone angle-triangle.

In the present work, momentum flux analysis is applied on two-single-hole GDI injectors to trigger the effect of flash-boiling. Furthermore, penetration rate as well as cone angle were calculated and compared with the results of high-speed imaging.

## CHAPTER 3

### EXPERIMENTAL SETUP

#### 3.1. Introduction

The present work aims to study the spray characteristics by means of momentum flux technique for both spatial and global level at flash-boiling conditions. Flash-boiling term refers to the evaporation of the fuel that happens when static pressure is lower than fluid saturation pressure at the same fluid temperature. High-speed imaging is used as an assisting tool for the momentum flux as well as a measuring tool for the cone angle and the respective penetration rate.

#### 3.2. Experimental Setup

##### 3.2.1. Schematic Diagram

In Figure 3.1 the schematic diagram of the momentum flux is presented.

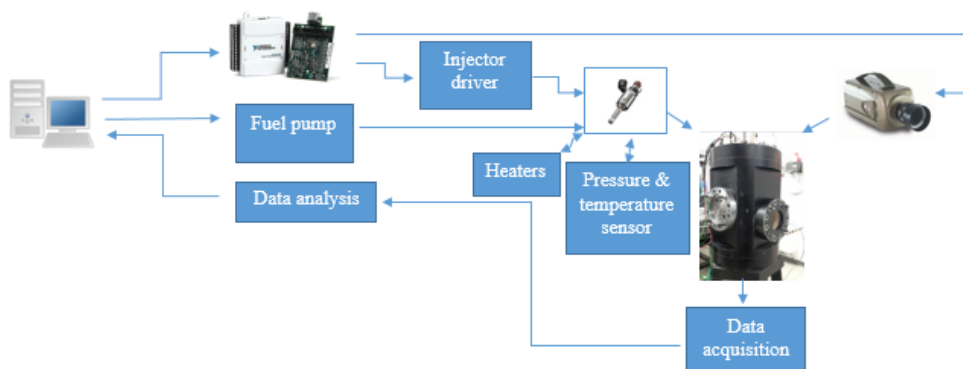


Figure 3.1. Schematic diagram for the momentum flux measurement technique.



### 3.2.2. Momentum Test Rig

The vessel is a chamber with a thick wall and four windows which facilitate seeing as well as installing the required fixtures inside it. However, both the wall and the windows are built in such a way to withstand with a pressure ranges from 0.3 to 85 bar to meet with the anticipated experimental conditions, see Figure 3.2.

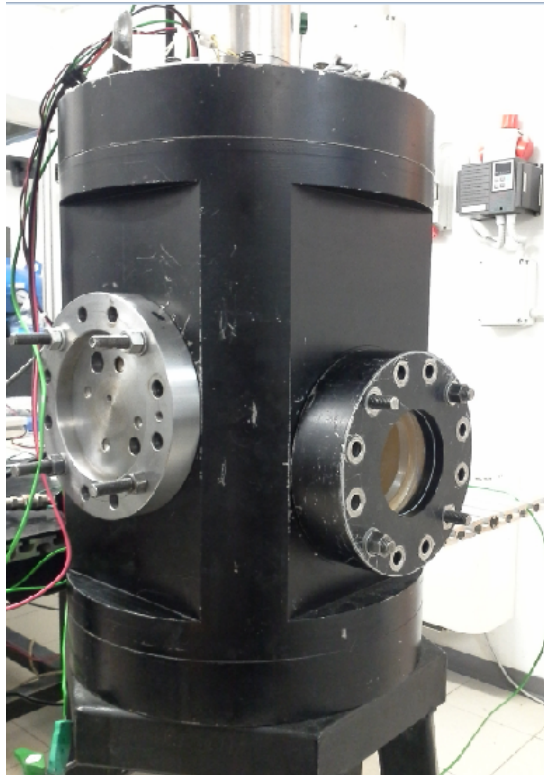


Figure 3.2. Momentum flux vessel.

The sensor-holding fixture has been prepared according to the dedicated injector in a way that the perpendicularity onto the target is guaranteed, see Figure 3.3.

As a complement to the required appliances for momentum flux tests, several devices are connected to the rig for accomplishing some missions such as injection pressure. A small pump is utilized to maintain a fuel pressure up to 6 bar, while another pump is used to achieve pressure up to 200 bar in addition to a 1:10 pressure converter-factor - multiplicador. A cylindrical container of 1 L volume is mounted to the injector in order to keep the percentage reduction of pressure after each injection below 1%. That cylinder works as a damper for the pump as well as attains the required injection pressure precisely.

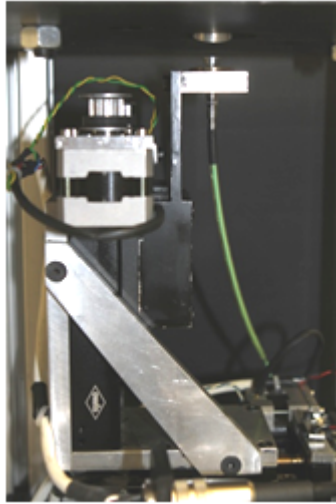


Figure 3.3. Momentum flux fixture and moving system.

### **3.2.2.1. Current Profile, Injector Control**

The injector is controlled via an electrical power supply which generates a suitable current profile corresponding to the needle-time-lifting postulated for the experiment. However, the current profile is setup using a kit-peripheral interface. Figure 3.4 resembles the several values for the current profile which draws the peaks and valleys in addition to some other factors.

### **3.2.2.2. Spatial Momentum Flux-Cone**

In order to acquire a slice from the jet, several cone-shaped single-holed spray dividers with different surface-angle, hole diameter were developed, tested and respectively verified by means of CFD analysis, see Figure 3.5. The cone of 2 mm hole-diameter suited the spray plume for all the spatial momentum flux test.

### **3.2.2.3. Target**

The target should be a little bit bigger than the jet in order to acquire all the jet and it should not be too larger to avoid the noise. Many targets have been tested to make sure that the readings are logically accepted and assured by the CFD results. Figure 3.6

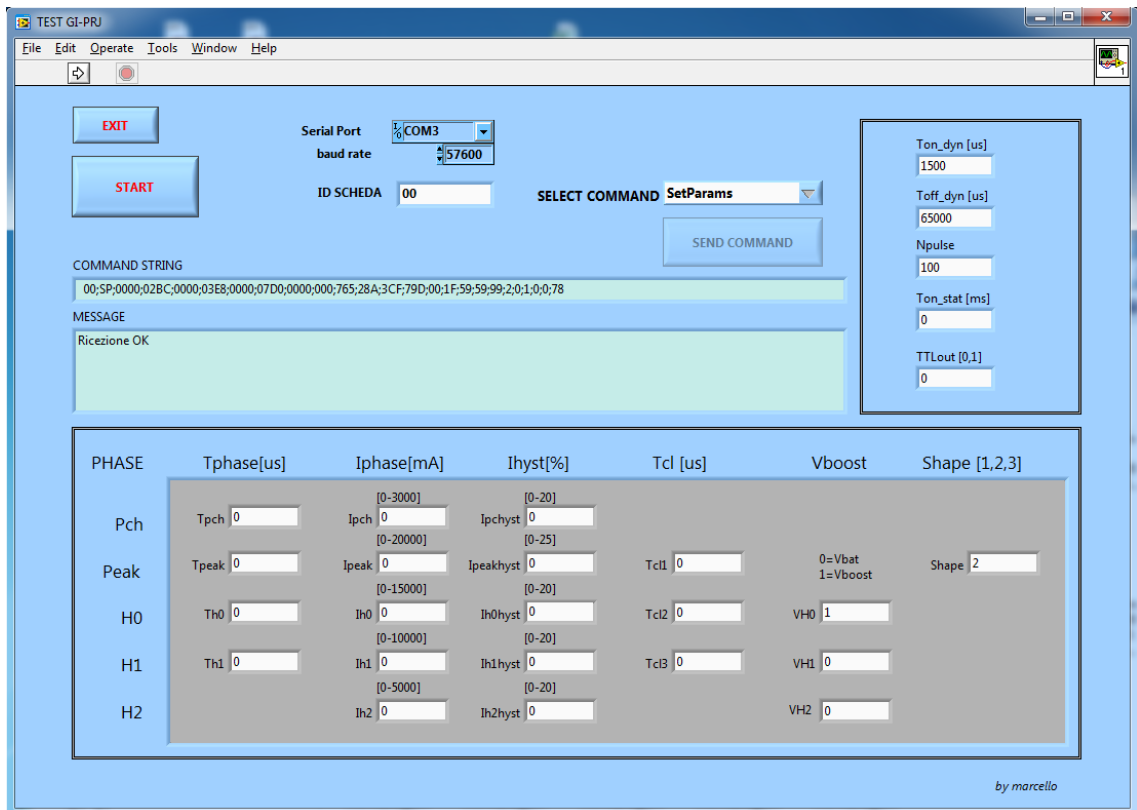


Figure 3.4. The values of the current profile.

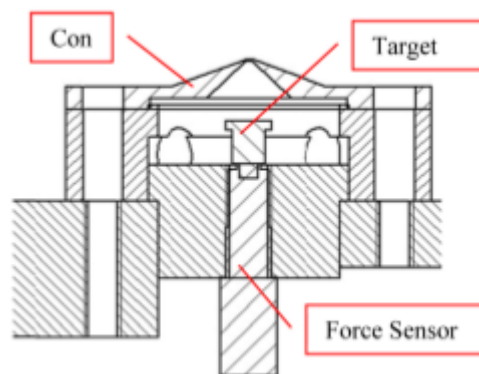


Figure 3.5. Spatial momentum test cone-fixture.

illustrates several proposed-shapes for the target. The target of '12' mm diameter suited the injector-jet for global test and of '8' mm for the local test.



Figure 3.6. Different target shapes.

### 3.2.2.4. Force Sensor

A Kistler force sensor connected to an amplifier was used, see Figure 3.7. However, the scale of the sensor was 1 Newton per Volt (N/V). To avoid the noise appeared in the force acquisition, two filters were used. Both filters were low-pass-filter type; the first one was 30 KHz located within the amplifier, whereas the second one was a software-based filter of 8 kHz.



Figure 3.7. Kistler force sensor.

### 3.2.2.5. High-Speed Imaging Technique

It is compulsory to achieve the perpendicularity as well as the coincidence among the cone-hole and the jet-axis. For this reason, high-speed video technique was utilized for centering and achieving the zero-position. Figures 3.8 and 3.9 illustrate the principle of alignment for both local and global test, respectively; as an example, the zero-position in a case of global test was (12.78:15.67:5.0) mm x,y,z, respectively.

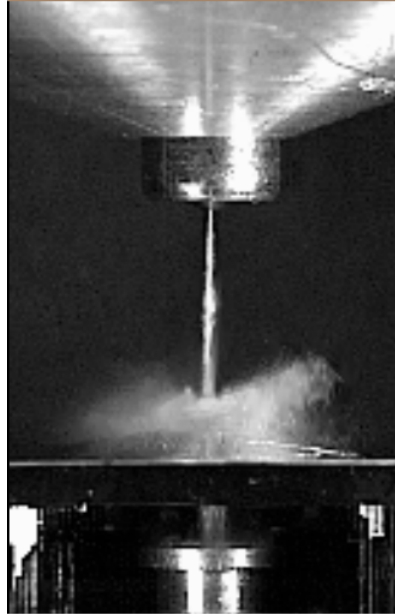


Figure 3.8. Centering for local test utilizing high speed imaging.

The movement in the 3-axes was accomplished by means of 3 stepper motors with a 200 steps per revolution. They were controlled via an interface assisting-program for each axis-direction, and thus, it gives the opportunity to save the home position for the force sensor as well as the park position , see Figure 3.10.

As the test fixture should be inserted inside the vessel, a feedback system is required. Figure 3.11 resembles a feedback interface which specifies precisely the distance covered by the steppers.

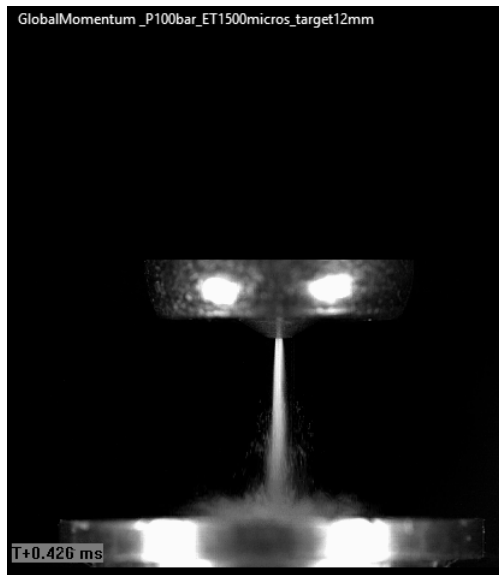


Figure 3.9. Centering for global test utilizing high-speed imaging-video technique.

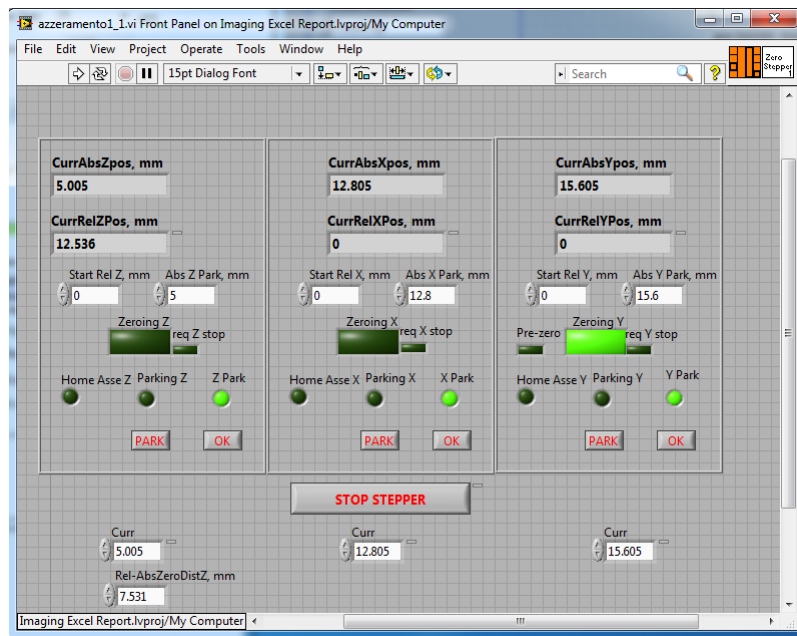


Figure 3.10. Zeroing program-interface.

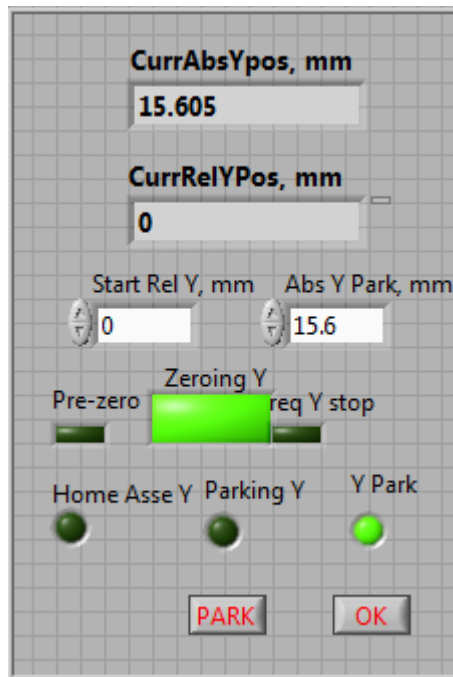


Figure 3.11. feedback control system interface.

### 3.2.3. Spray Penetration

Momentum flux measurements provide a well-predicted penetration rate value which is comparable with the ones calculated by means of high-speed imaging technique. The penetration rate using high-speed imaging is calculated by relating the values of the jet-tip length to its corresponding time rate. On the other hand, it is calculated by tabulating the time at which force-acquisition commences versus the distance from the target.

### 3.2.4. Cone Angle

Cone angle can be calculated utilizing the local momentum flux results in accompanys with the images. Figure 3.12 illustrates the concept. A reference comparison can be made among the results that have been achieved utilizing the local momentum flux test with the ones of high speed imaging technique providing that the value calculated by the local test is always less than of that from the images.

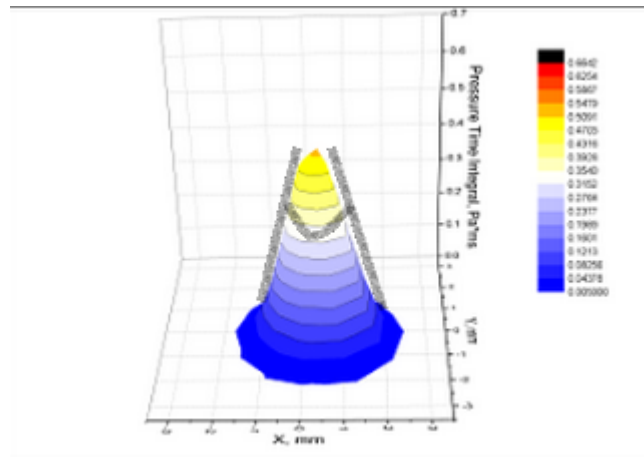


Figure 3.12. Calculating cone angle utilizing spatial momentum results.

### 3.3. Experimental Procedure

Starting with the Design of Experiment (DOE) concept, a test plan was created carefully to acquire the flash-boiling phenomenon in specific operating conditions. Before setting the fuel pressure to the required value, a low pressure pump was turned on; in order to suck the fuel from the tank. Later on, the intended injection pressure was set using a high-pressure pump via a Labview-environment self-developed interface. An order from the computer utilizing a self-developed program in the labview environment was sent to a National Instrument (NI) device which sent a signal to the injector driver to create a suitable current profile fitted the injection requirements in terms of the start-of-injection time, duration, frequency, etc. Further, the NI device synchronized the signal with the high-speed imaging camera to commence detecting once the injection occurs. Two or more heaters (depends on the need) were inserted into the container just before the injector in order to heat the fuel and another set of heaters was installed just near the injector to heat up the nozzle. It is worth to point out that a pressure sensor was inserted just before the injector in order to measure the fuel pressure before leaving the nozzle. After that, the spray was injected into the so-called vessel that can withstand both vacuum and pressure as well. The momentum test rig which consists of a force sensor, target plate, positioning system, etc. was installed inside the vessel and fixed properly. The force sensor detected the spray injected over a several distance planes from the nozzle for the global momentum flux and over a group of points called (map) with different vertical distances for the spatial momentum. The signal detected by the force sensor was amplified and filtered. Later on,



it is visualized on a Labview environment self-developed program interface. For each test of global momentum, the output was a set of six word-document files( 1 file per distance). However, there were about more than 40 word files for a spatial momentum test. After that, excel is used to analyze the results for global momentum flux while Origin software is used to post process the measurements and gives several formats for the results.

### 3.4. Experimental Strategies

The so-called Air to Saturation Pressure Ratio (AtSPR)'s, for the nine experimental conditions are reported in Table 3.1, whereas the ranges at which flash-boiling is partially, fully or not exist at all is shown in Table 3.2.

Table 3.1. The working condition with the corresponding AtSPR-values.

Source: (Xu et al., 2013)

Vessel Pressure KPa	Fuel Temperature °C		
	30	90	120
40	8.47	0.51	0.22
101	21.38	1.28	0.55
303	64.16	3.85	1.65

Table 3.2. Ranges of ASPR for flash-boiling effect.

AtSPR <0.3	Full Flash-Boiling
0.3 <AtSPR <1	Transition Zone
AtSPR >1	No Flash-Boiling

According the concept of research and DOE principle, two single-hole injectors with different L/D parameter, see Table 3.4 , were investigated over both flash-boiling point and non flash-boiling point conditions. The temperature of the nozzle-tip and fuel together were varied over three values, three values of ambient pressure, three values of injection pressure and two energizing times were set. Both Global and spatial momentum analysis were performed for all the test-conditions specified in Table 3.4.

To achieve the repeatability in the global momentum flux, the test was repeated at least 40 injections for each plain-distance, from the nozzle, as followed (over Z-axis): 5, 10, 15, 20, 30, 40 mm. However, for spatial momentum flux test, the concept of reliability

Table 3.3. Injectors specifications.

Injector name	L/D
IHP 279	1
IHP	3

Table 3.4. Generic test plan for different pressure, temperature and energizing time conditions.

Energizing time = 1-3 ms									
Injection pressure	30 °C			90 °C			120 °C		
	40 <i>kPa</i>	101 <i>kPa</i>	303 <i>kPa</i>	40 <i>kPa</i>	101 <i>kPa</i>	303 <i>kPa</i>	40 <i>kPa</i>	101 <i>kPa</i>	303 <i>kPa</i>
50 bar									
100 bar									
150 bar									

was achieved via replication of at least 30 injections for each point in the predefined map, which consisted of approximately 180 points over two different plain-distance. The number of points varies according to the coverage of the map; for instance the map of Z=30 mm was quite larger than of Z=10 mm. At flash-boiling conditions, the points should be more than that of the non flash-boiling map. Furthermore, to achieve the steady state, 10 injections were done at each position-condition before acquiring the force.

## CHAPTER 4

### RESULTS

#### 4.1. Spray Momentum Flux

##### 4.1.1. Global Momentum Test

Injectors are manufactured in different ways for specific purposes such as improving the mixing capability via widening the cone angle. Among those differences, the parameter  $L/D$  is one of the most predominant parameters. However, the tested injectors are of 1 (IHP-279), 3 (IHP-293) ( $L/D$  coefficients). The  $L/D$  coefficient reflects the path of the spray jet before fuel issues from the nozzle.

In the scope of momentum flux study, several parameters will be studied and analyzed in order to comprehend the spray general-shape and the internal structure as well. Among those parameters momentum flux itself, i.e. the indirect-measured-force, and cone angle as well as penetration rate will be investigated in details.

The test plan 3.4 was followed for both injectors. Figure 4.1 shows the effect of the quiescent pressure on the measured-force as well as the different response for each injector over the following conditions: Energizing Time (ET)=1.5 ms, Fuel Temperature ( $T_f$ ) =30 °C, Tip Temperature ( $T_p$ )=30 °C, Vessel Pressure ( $P_v$ ) =40 KPa, Injection Pressure ( $P_{inj}$ ) =100 bar, Sensor Distance ( $Z$ ) =10 mm. The end of acquisition for the IHP-293 ( $L/d=3$ ) injector is obviously more than that for IHP-279 ( $L/D=1$ ) since  $L/D$  is larger. Thus, the length of the nozzle, increases friction losses and reduces the flow speed. It can be seen that the measured force, generally, is higher for the  $L/D=1$  injector than that for  $L/D=3$ . Further, the nozzle for the  $L/D=3$  injector is respectively longer than for  $L/D=1$  and therefore, friction losses will be higher as well, which can be referred as the hydro-dynamical effects. Moreover, the end of acquisition is dramatically affected by the vessel ambient pressure; going towards the 303 KPa, it can be inferred that the quiescent pressure slows down the spray to reach the target.

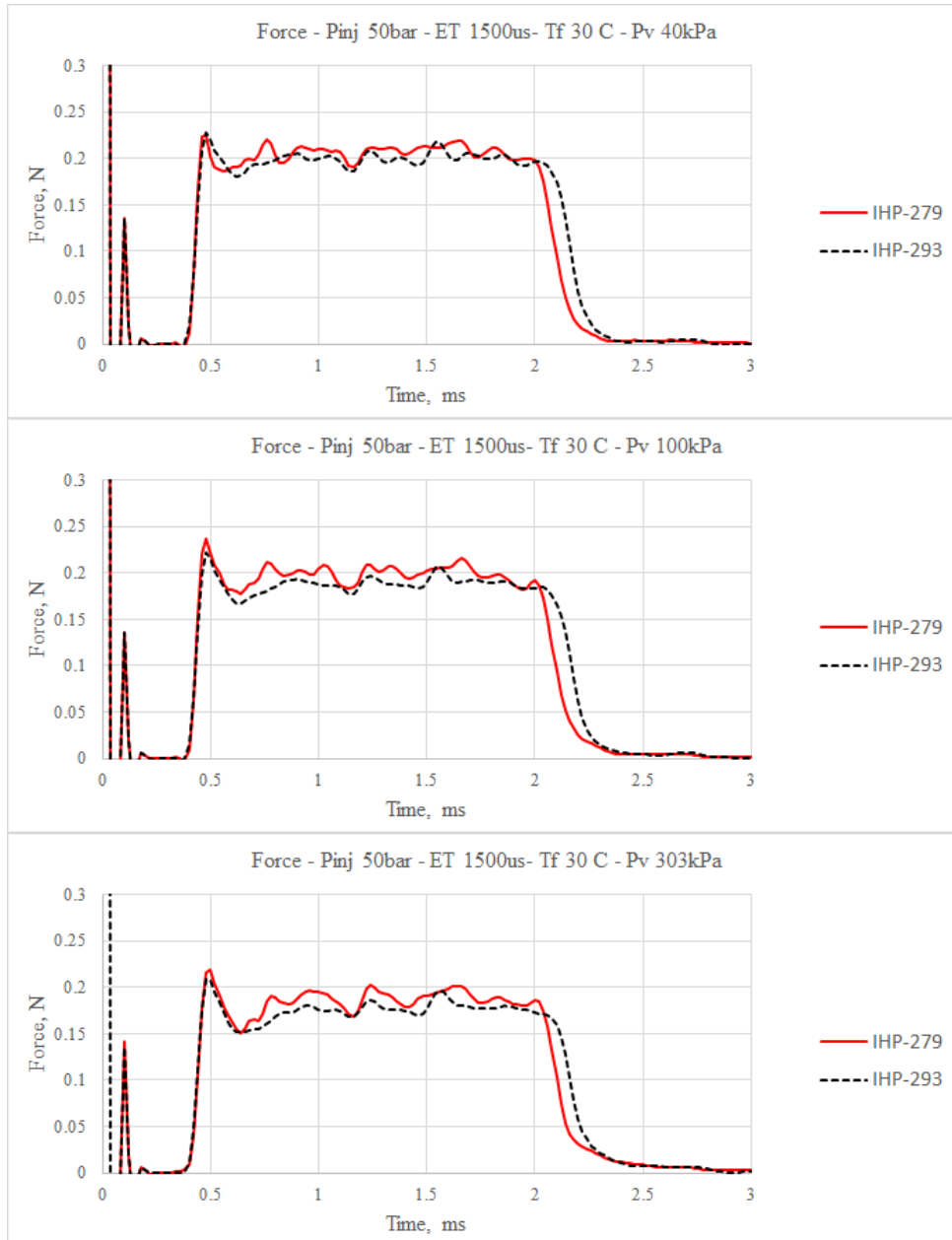


Figure 4.1. Effect of vessel pressure on the detected force on IHP-279, IHP-293 injectors.

It is worth to mention that the precedent signal which is sensed at the time of 0.12 ms can be referred as an error or noise in the sensing device. The peak signal at the time approximately 0.5 ms can be attributed to two facts: the first one is that the initial spray drops are larger than the following ones. The second fact is that the air induced between the nozzle jet and the force target, which can be apparently noticed in the vacuum to pressurized ambient pressure in which the aforementioned peak becomes larger when compared to the adjacent one.

The results of the injector IHP-293(L/D=3) are slightly more straight in sense of having less peaks and valleys in the stable region than of the IHP-297(L/D=1) injector. This can be attributed to the fact that the longer nozzle-tube makes the flow narrower and more homogeneous which appear at all the conditions, see Figure 4.1

Figure 4.2 elucidates the force measured at  $T_f=120\text{ }^\circ\text{C}$  for the two injectors. Starting from the initial measured-signal, it can be seen that there is a signal before the time approximately 0.4 ms, it is triggered in all the measurements, which can be accepted as an error or noise in the sensing transducers, and thus, it will be canceled in the following figures. The peak at  $T=0.5$  ms in the first figure of Figure 4.2, which is a flash-boiling condition, is dramatically less than of the other conditions in the same figure, which can be inferred to the vapor content that hinders and slows down the spray flow.

The effect of L/D parameter is predominant at both high and low fuel-temperature. The force experienced at the L/D=3 is appreciably less than of L/D=1 due to the hydrodynamical friction losses. The end of acquisition is precedent for IHP-279 (L/D=1) due to the longer nozzle-length. However, the peak of the measured-signal at the beginning is apparently fully diminished while flash-boiling plays the main role. Whereas at a partially flash-boiling presence, at  $P_v=101$  KPa the peak is a little bit less than the one at low temperature, see Figure 4.2. The vapor content in the spray can be the cause for the non-existence of the peak at the beginning of the stability region for the fully flash-boiling condition, and dramatically decreasing it for the partially flash-boiling condition.

The effect of the quiescent pressure and fuel temperature, both injectors are alike in several trends, except for small differences in the detected force value, smoothness and end-of-acquisition time. IHP-293 is more widely-commercially-used than the IHP-279 because of its spray characteristics and air/fuel mixing capabilities. However, IHP-293 has a L/D=3 while IHP-279 has a L/D=1 which make the jet of the bigger L/D to be more controlled and directed, even though the spray in the L/D=3 may loose some of its strength as a friction loss in the nozzle. Therefore, the following results will be mainly concentrated on this injector.

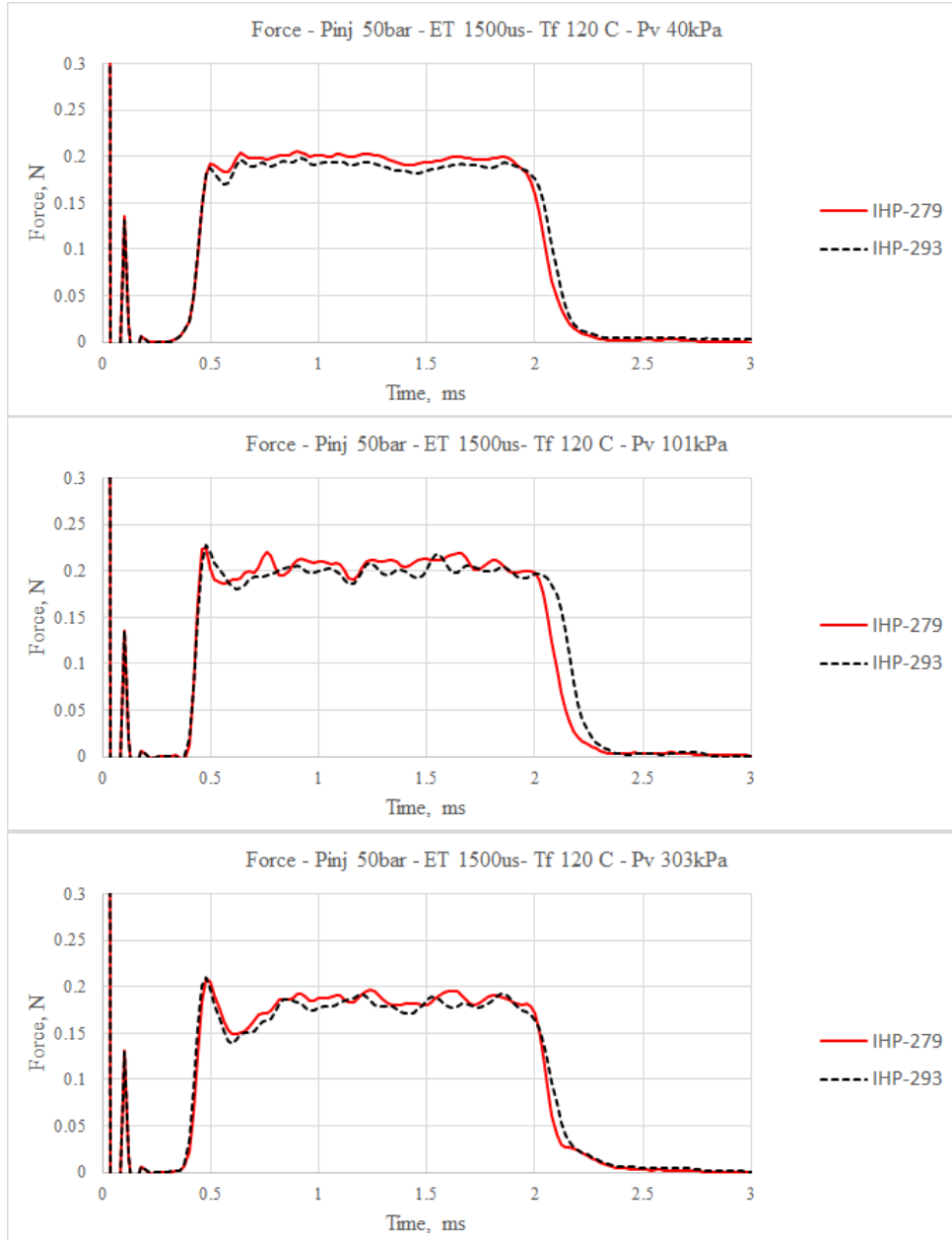


Figure 4.2. Comparison among IHP-279, IHP-293 injectors under flash-boiling effect.

The injection pressure effect can be detected by means of momentum flux measurements. Figure 4.3 illustrates the effect of injection pressure at low temperature condition. At the beginning of acquisition a similar summit appear at the three injection pressure for all the quiescent pressure values. It can attributed to the interaction between the spray and the air induced in the space just on the top of the target. Moreover, the increment of the detected-force corresponds to the injection pressure: the higher the injection pressure is, the higher the force is detected. The force is slightly higher when moving from in-pressure to vacuum vessel condition, at the same injection pressure, which can be attributed to the fact that spray is affected and hindered by the existence of the air.

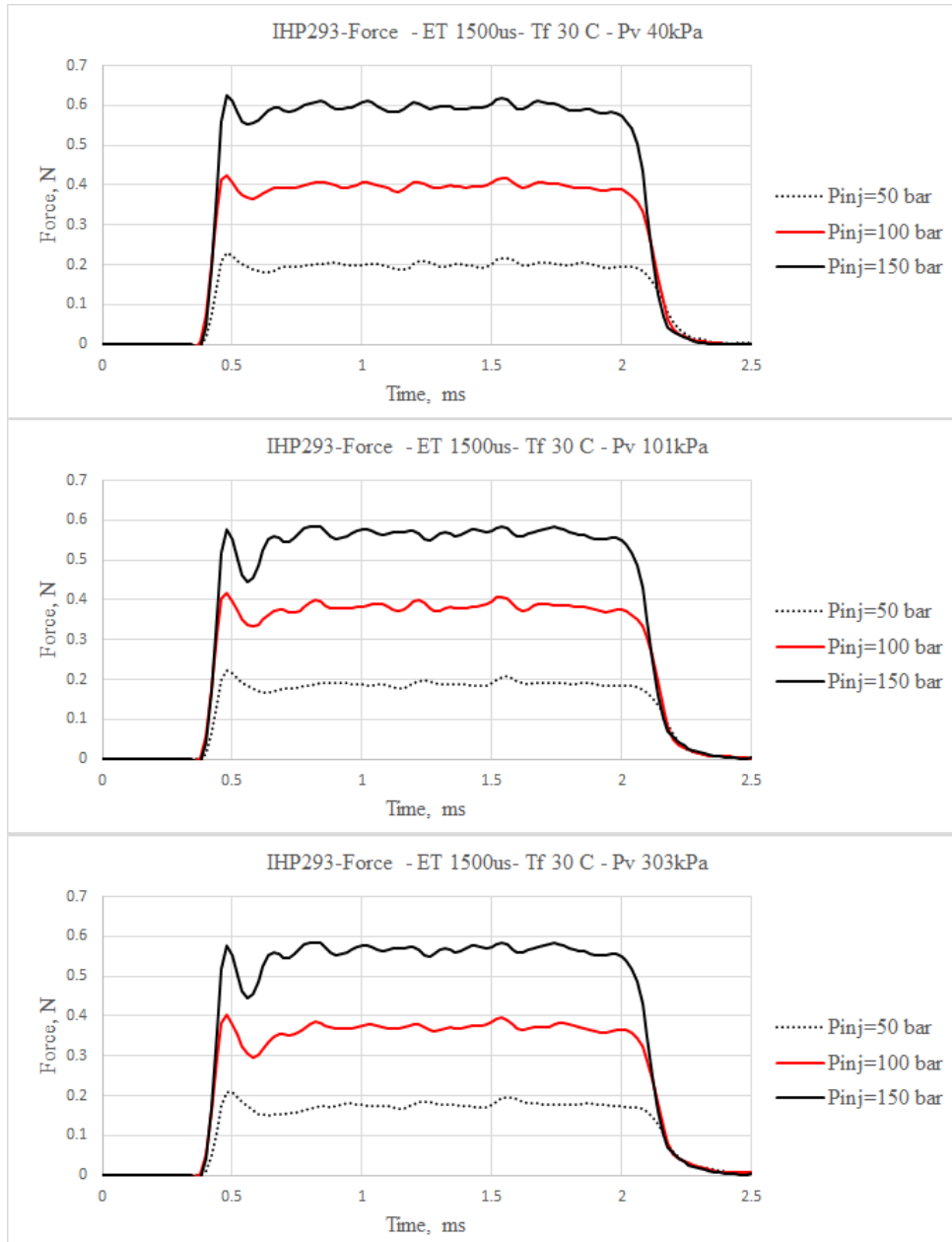


Figure 4.3. The effect of injection pressure over different vessel pressure at non flash-boiling condition.



Figure 4.4 resembles the effect of the injection pressure at high temperature where flash-boiling phenomenon can be triggered. At the first figure, fully flash-boiling condition is detected; the summit at the beginning of stability stage is diminished and substituted with a small step, which can be attributed to the participation of the vapor with the spray itself while impinging the target. In the second part for of Figure 4.4, a partially flash-boiling condition can be detected. The summit at the beginning of the stability stage is dramatically less than that for the non flash-boiling condition, (second part of Figure 4.3, which can be attributed to the vapor content.

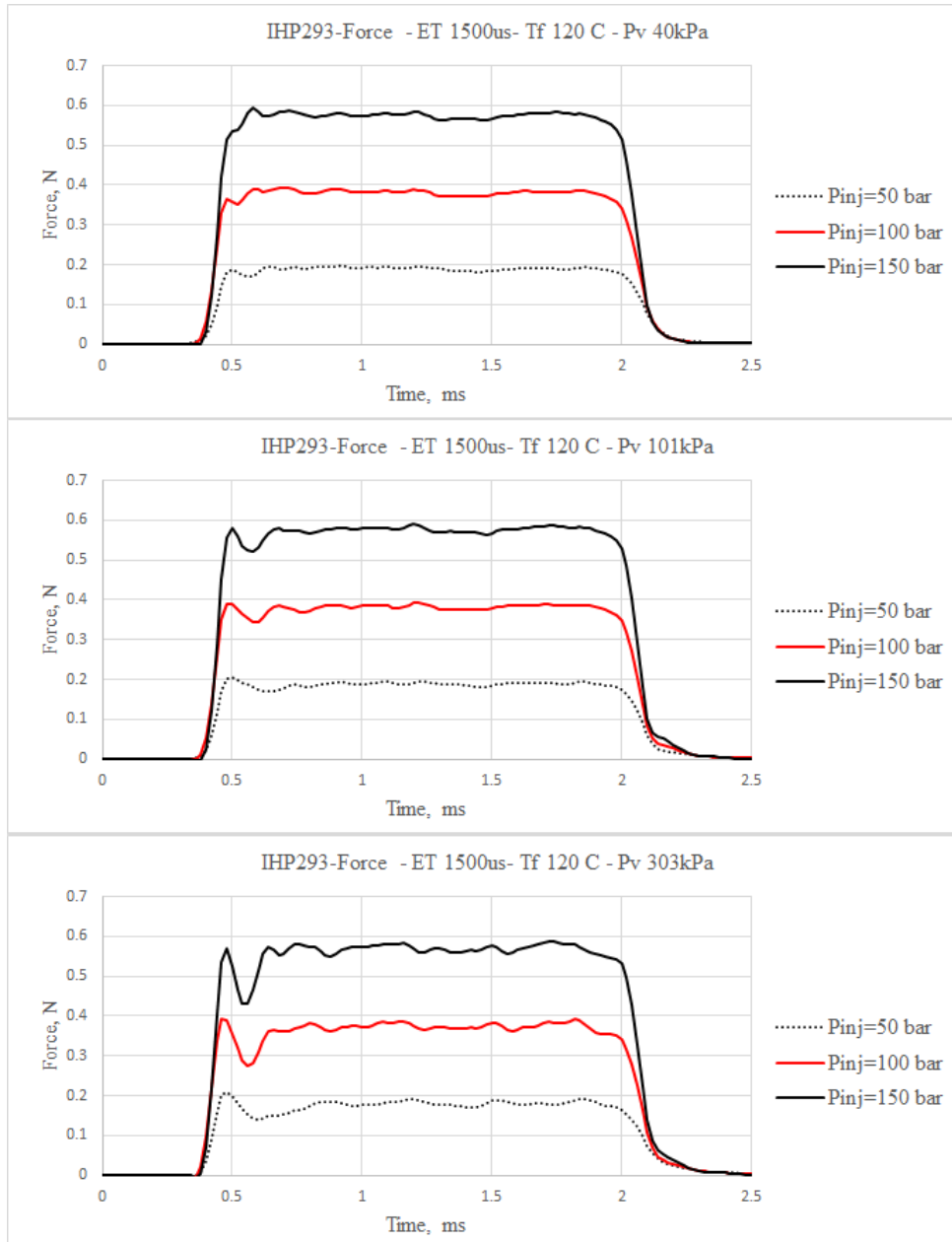


Figure 4.4. The effect of injection pressure over different vessel pressure at flash-boiling condition.

Figure 4.5 illustrates the effect of energizing time on the detected force. It is seen that the peak at the beginning of the stable region decreases as the vessel pressure increases. A general decrement in the stable region is noticed when the vessel pressure increases due to the pressure on the spray. However, there is an overlap up to the 2 ms among the 1500  $\mu$ s and 3000  $\mu$ s for all the figures, which is almost half the way of the 3000  $\mu$ s detected force.

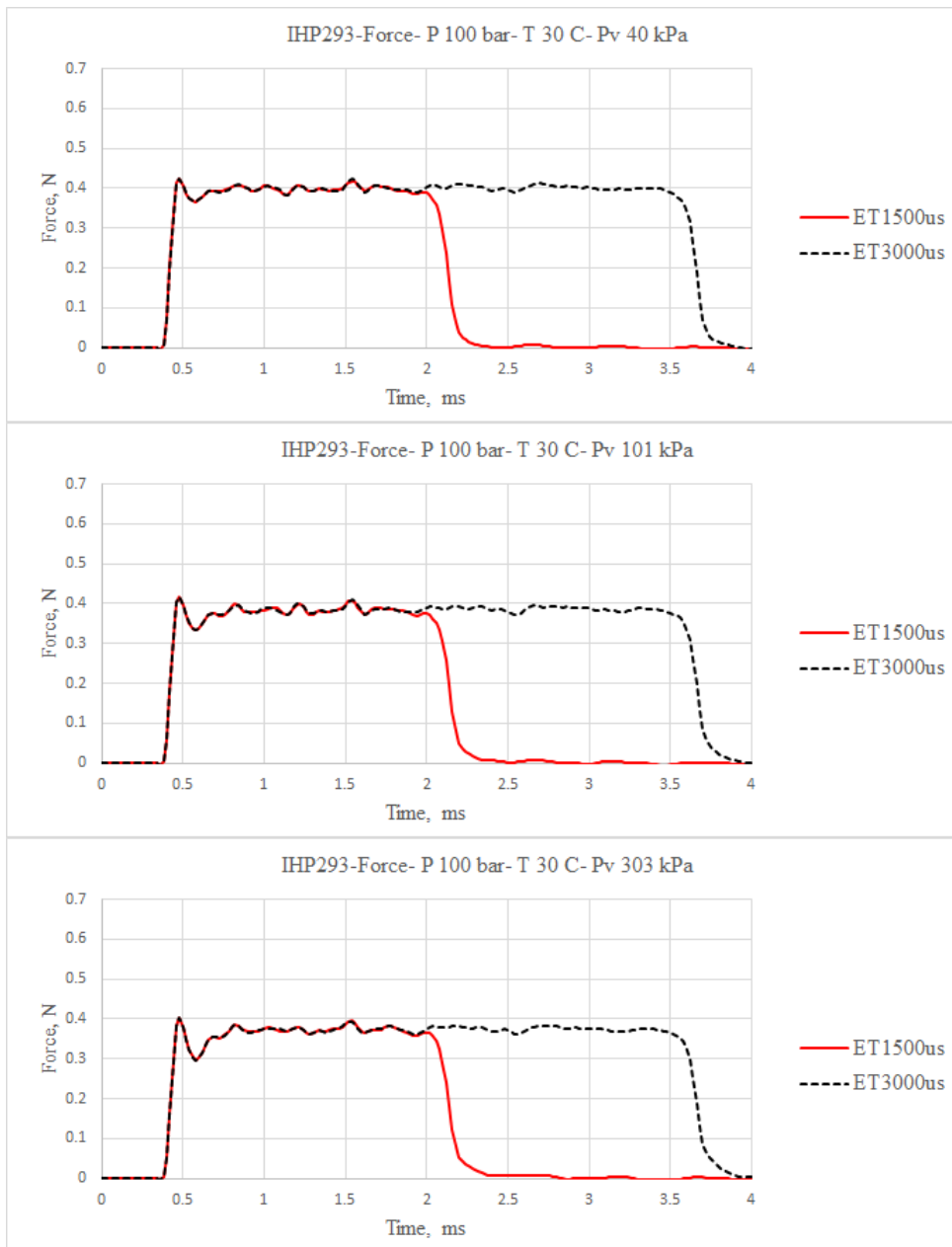


Figure 4.5. The effect of energizing time at Tf 30 C over different vessel pressures.

However, Figure 4.6 presents the effect of energizing time on momentum flux at fuel temperature  $90\text{ }^{\circ}\text{C}$ . The overlap is seen from the starting of injection up to the 2 ms time, which is the mid-point among 1500, 2000  $\mu\text{s}$  energizing times for all figures. A general decrement in the momentum is detected when the condition is changed from the vacuum to the in-pressure vessel pressure, which is kind of consistency regardless to the fuel temperature. It is noteworthy to mention that the  $90\text{ }^{\circ}\text{C}$  fuel temperature can be representative to show the effect of the energizing time at elevated temperature.

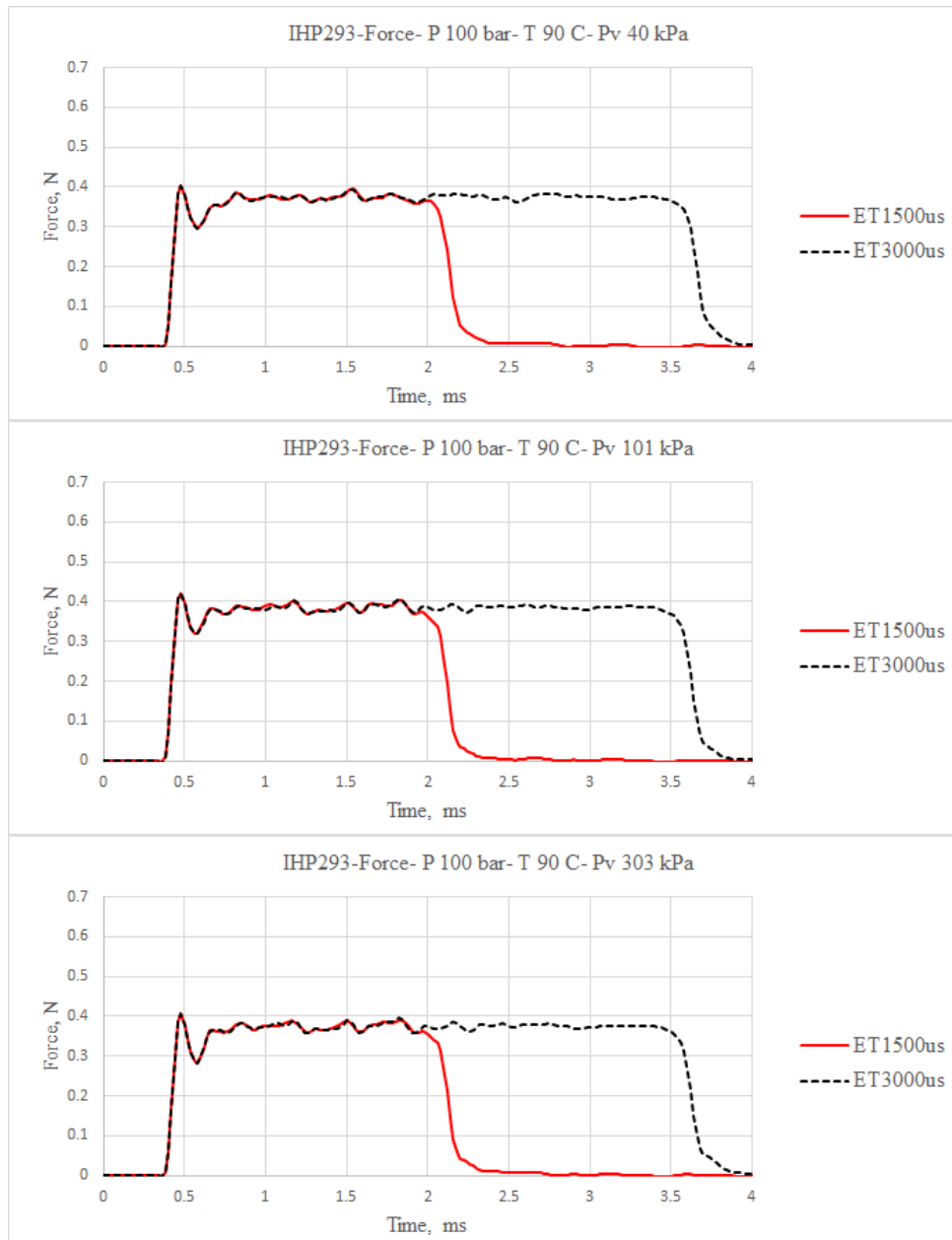


Figure 4.6. Effect of energizing time at 90 C fuel temperature.

It can be seen that the detected-force at high fuel temperature is slightly less than of that at low fuel temperature; at the first figure of Figure 4.4 with its corresponding figure at Figure 4.3. Flash-boiling phenomenon can explain the difference due to the vapor content which hinders spray forefront and, hence, decreases its average value. In the other figures, it may be interpreted as a molecular interactions due to the high temperature, which results in a loss in the average spray-force value. Furthermore, it can be noticed that the acquisitive-force is smoother due to the vapor presence.

In the precedent figures, the injection pressure is 50 bar while in the following figures it is 100 bar. At both injection pressures, the injector behaves in a similar way and , thus, 100 bar injection pressure has been chosen to be the representative value.

Figure 4.7 illustrates the effect of the  $Z$ . However, the delay in reaching the target can be easily triggered whatever the conditions are because of the time needed for the spray to reach the target. In the stability region, i.e. 0.7 - 2 s, it is shown that some instability signal or noise is triggered. However, the experienced-instability, is slightly more for the distance  $Z = 30$  mm than of that at the distance  $Z = 10$  mm, which may be attributed to the interaction between spray and its surroundings. Moreover, it is clear that the force detected in the transient period is slightly delayed to the right, for both distance 10 and 30 mm as well, when moving from vacuum to in-pressure vessel pressure. However, this can be attributed to the effect of the quiescent pressure which hinders, and thus, decelerates spray and reduces its average momentum-value as well.

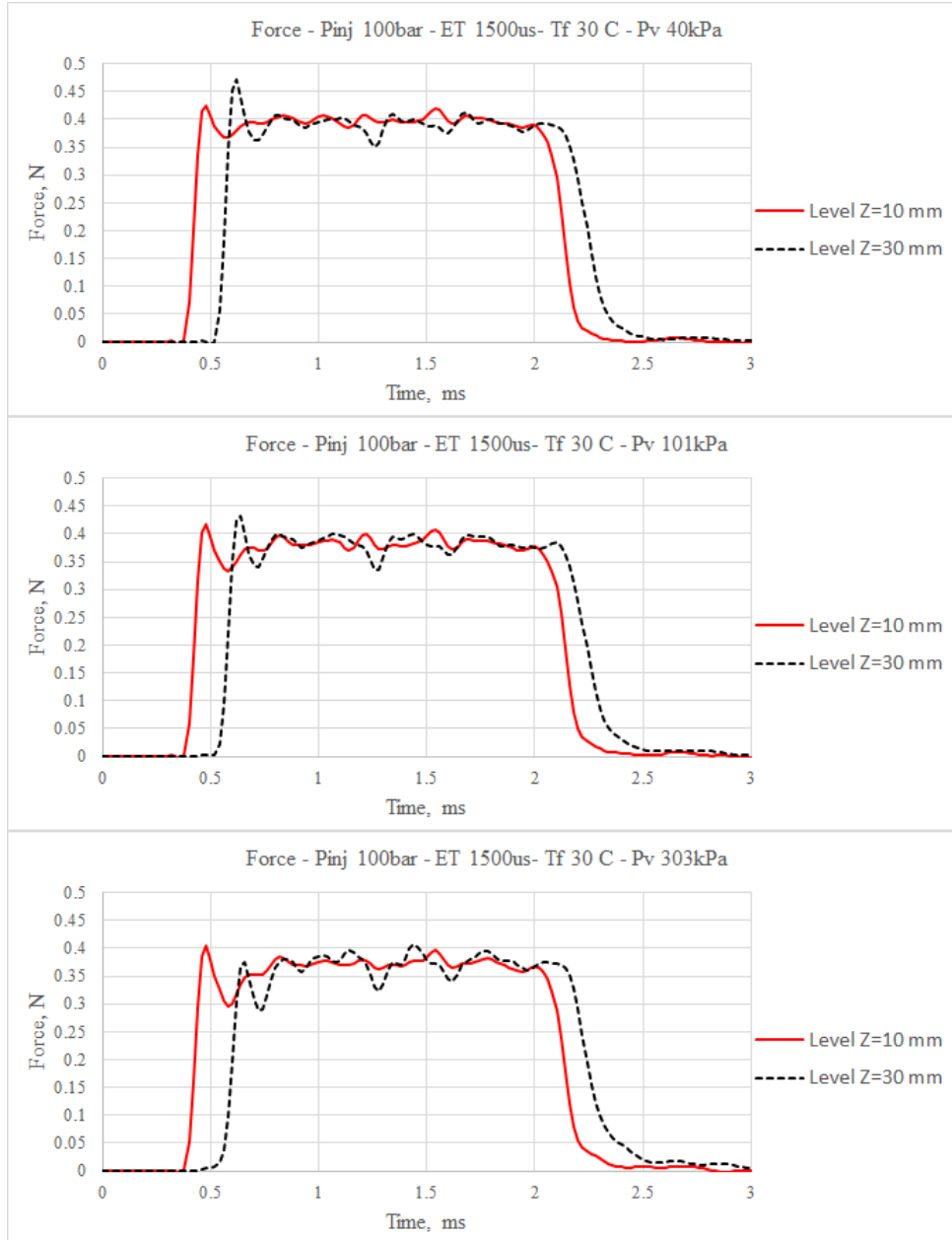


Figure 4.7. Comparison among the height distance Z for IHP-293-P100,ET1500,Tf30

Figure 4.8 illustrates the effect of the distance  $Z$  on the detected force. In the first one, fully flash-boiling condition is triggered,  $At_{SPR} < 0.3$ , whereas in the second figure a partially flash-boiling is detected. It is seen that at flash-boiling condition the peak at the beginning of the stability period is drastically decreased due to the vapor participation. Moreover, the delay experienced at distance  $Z=30$  mm is more than that at the low temperature condition; since the jet has larger cone angle and respectively larger size, and thus, it can be inferred that the jet is subjected to more air resistance which in turn results in a delay in reaching the target.

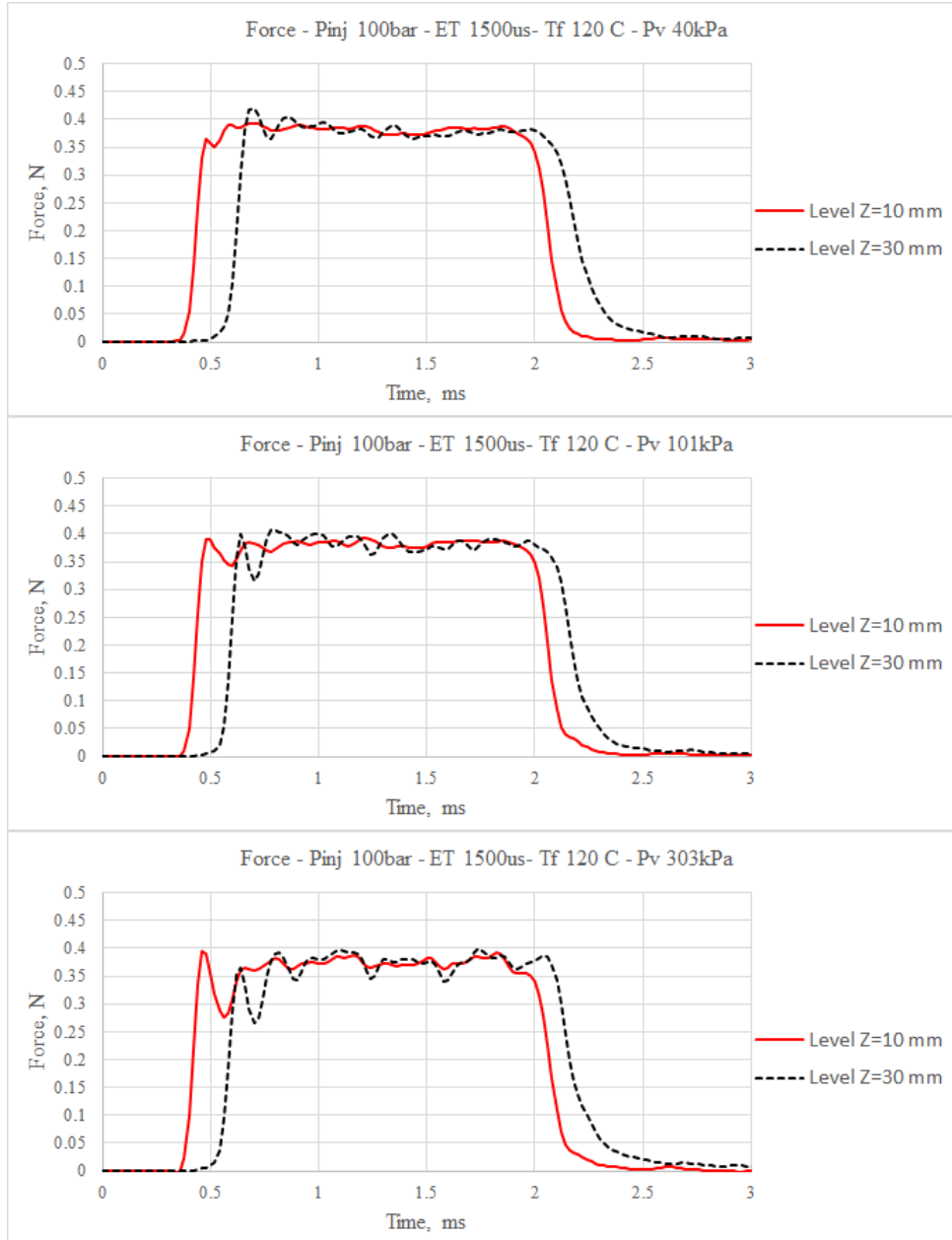


Figure 4.8. Comparison among the height distance Z for IHP-293-P100,ET1500,Tf120



All the following figures are based on the distance  $Z=10$  mm value which is chosen to be the representative one. The aim of choosing it is to study the spray in the nozzle near-field which has less surrounding effect.

Figure 4.9 illustrates the effect of fuel temperature under different vessel pressure values focusing on the transient force-triggered region. At the first figure, it is seen that spray arrival time is almost overlapped at the three fuel temperatures, and the value of the force detected at fuel temperature  $30\text{ }^{\circ}\text{C}$  is slightly higher than the others. The reason behind that may be expressed as losses in the fuel due to the molecular interactions at high temperature values such as  $90$  and  $120\text{ }^{\circ}\text{C}$ . In the second and third figures at injection-closing region, the acquisition at fuel temperature  $120\text{ }^{\circ}\text{C}$  ends earlier than the others, which may be attributed to the energy-induced in the fuel due to the elevated temperature. It is also clear that the measured force in the stability region is quite overlapped, which can be attributed to the effect of the vessel pressure.

Figure 4.10 shows the magnified transient part of Figure 4.9. The first figure shows a fully flash-boiling condition behavior. The second shows it partially whereas the third does not show it at all. As it is seen, in the fully flash-boiling condition, the summit of the detected-force at the end of the transient region decreases correspondingly to the increase of the fuel temperature; due to flash-boiling effect and the vapor induced in the spray. There is a nuisance translation in those peaks by moving from low-to-high temperature due to flash-boiling condition in which vapor content in the spray decelerates its arrival towards the target. However, in the partially flash-boiling condition the peak of the force at fuel temperature  $120\text{ }^{\circ}\text{C}$  is tilted a little bit, which means the spray arrives a bit later than that at other fuel temperature values because of the flash-boiling effect. In the third figure, an overlap of the summit is seen, which may be attributed to the absence of flash-boiling and the predominance of vessel pressure over fuel temperature.

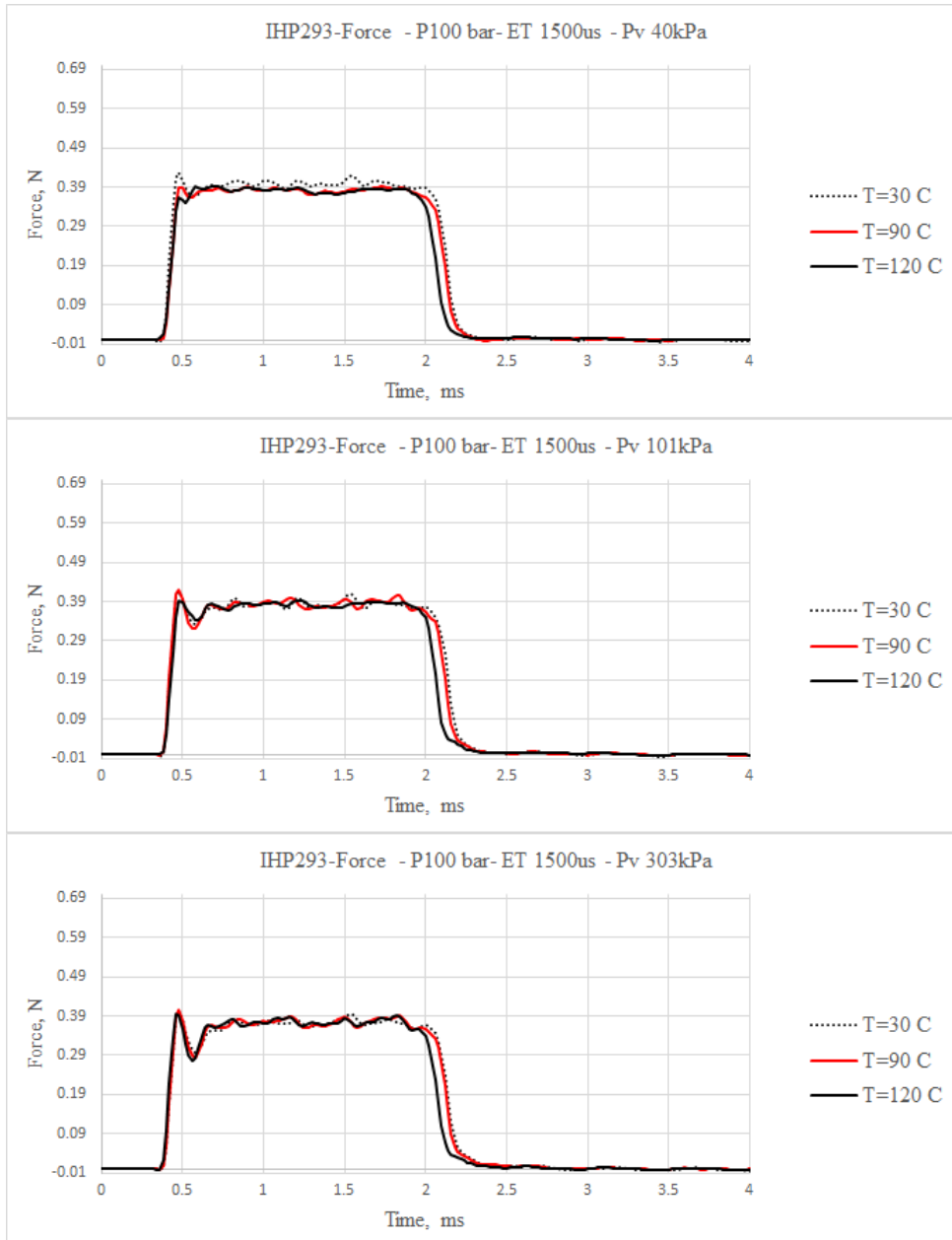


Figure 4.9. Effect of fuel temperature over different vessel pressure at distance Z=10 mm.

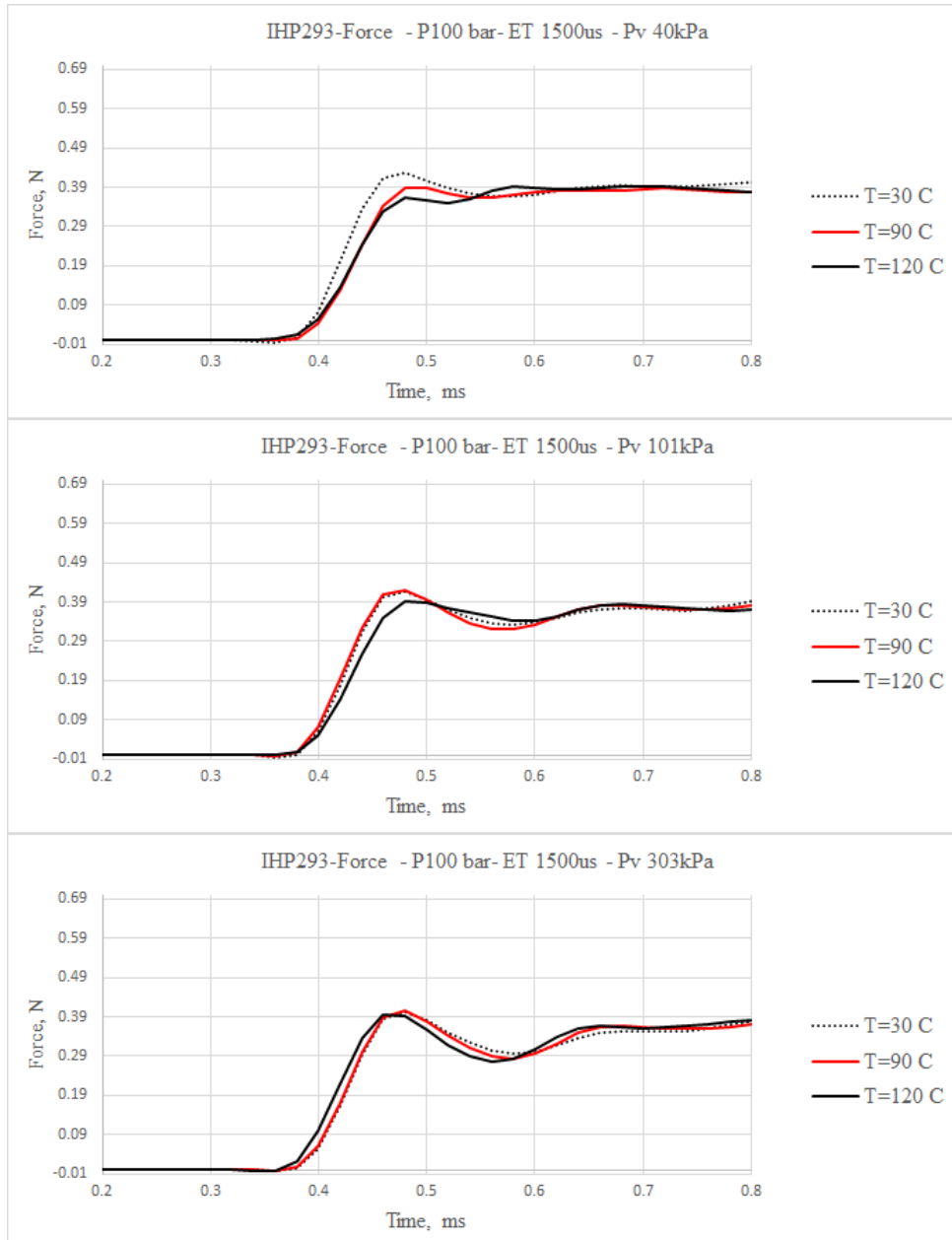


Figure 4.10. Magnification of the effect of temperature on the spray over different vessel pressure at distance  $Z=10$  mm.

At a longer  $Z$  the delay of the spray to reach the target can be clearly triggered. Figure 4.11 shows the effect of fuel temperature on different vessel pressure values. As seen in the first one, the average force detected at fuel temperature  $120\text{ }^{\circ}\text{C}$  is less than that of  $90\text{ }^{\circ}\text{C}$  and so forth, which can be attributed to the flash-boiling condition in which spray contains vapor. Therefore, it makes a kind of obstacle against spray coming out from the nozzle towards the target and thus the spray loses part of its strength. It is interesting to notice that the force detected at fuel temperature  $120\text{ }^{\circ}\text{C}$  is delayed to be the last one amongst the three fuel temperature values during the injection-opening stage, whereas it is triggered as the first signal in the injection-closing stage. However, at the opening triggered-signal the vapor induced in the spray interacts, and hence hinders and delays the spray-arrival time appreciably. At injection-closing triggered-signal instead, vapor makes an obstacle against spray issuing from the nozzle. After injection is closed it will not be any spray to push the vapor more. Therefore it finishes detecting earlier.

On the other hand, the second and the third figures are consistent in both injection-opening and stability periods. However, a peculiar behavior is seen for the fuel-temperature  $120\text{ }^{\circ}\text{C}$  at the injection-closing stage. The closing-time precedes for  $120\text{ }^{\circ}\text{C}$  that for the other temperatures, which may be attributed to the interactions in the molecular level as it was discussed for Figure 4.9.

To follow the transient signal at the injection-opening period, Figure 4.12 illustrates a magnified figure for the effect of the fuel temperature over different vessel pressure at  $Z=30\text{ mm}$ . It is noteworthy to mention that at distance  $Z=30\text{ mm}$  the participation of the vapor can be detected clearer than that at  $Z=10\text{ mm}$ . At the first figure, the peak of the force signal is translated to the right-side when moving from low-to-high temperature due to flash-boiling effect in addition to a slight decrement in the obtained-force gradually increasing from  $30\text{ }^{\circ}\text{C}$  to  $120\text{ }^{\circ}\text{C}$  for the same reason. On the other hand, at a vessel ambient pressure  $101\text{ KPa}$  where flash-boiling effect is partially detected, and thus a nuisance translation of the peaks is seen over the three temperature values gradually from  $30\text{ }^{\circ}\text{C}$  to  $120\text{ }^{\circ}\text{C}$ . Moreover, it is shown that the measured force is decreasing when moving from vacuum up to in-pressure quiescent pressure, which resembles the effect of vessel pressure on the spray evolution.

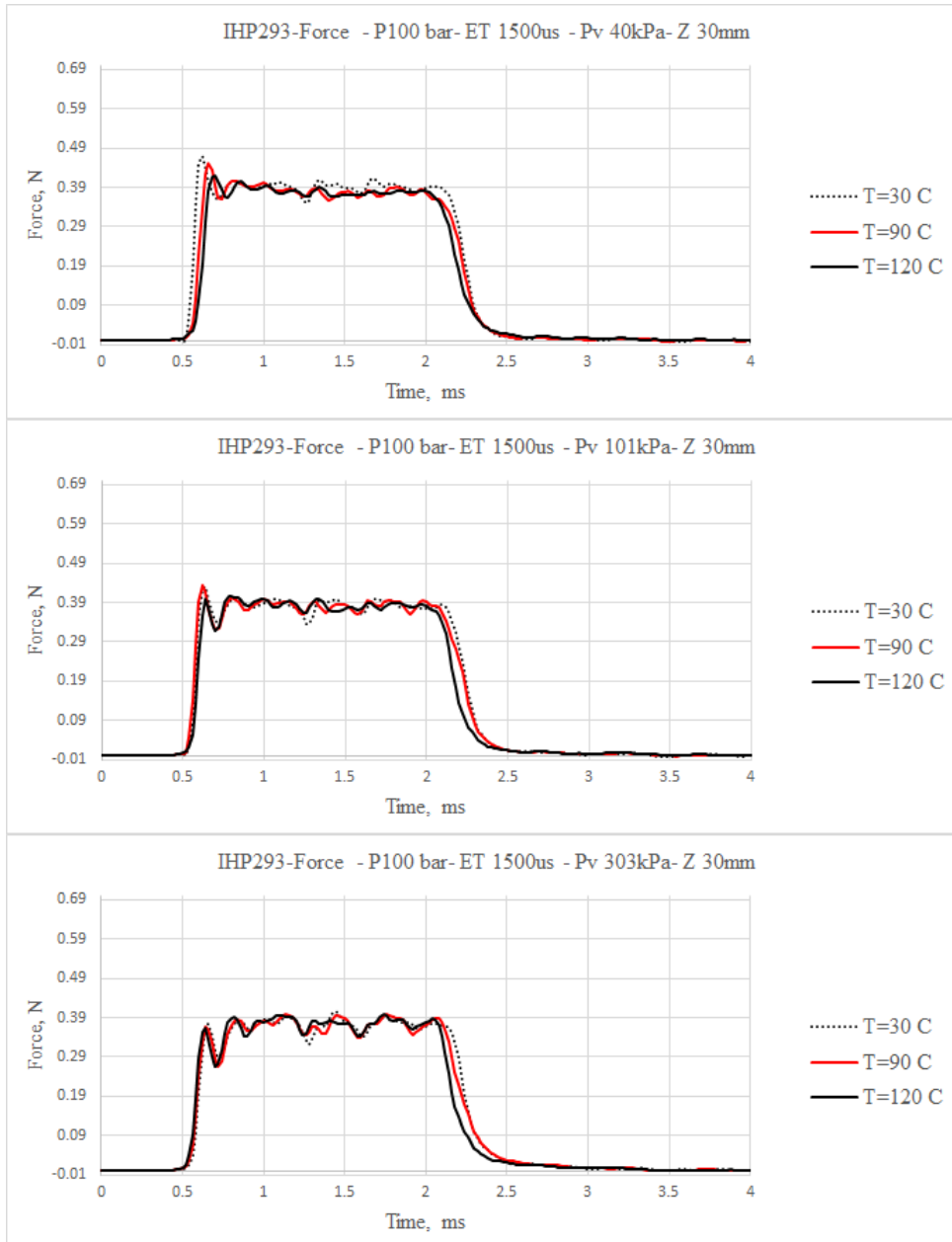


Figure 4.11. Effect of temperature on the spray over different vessel pressure at distance Z=30 mm.

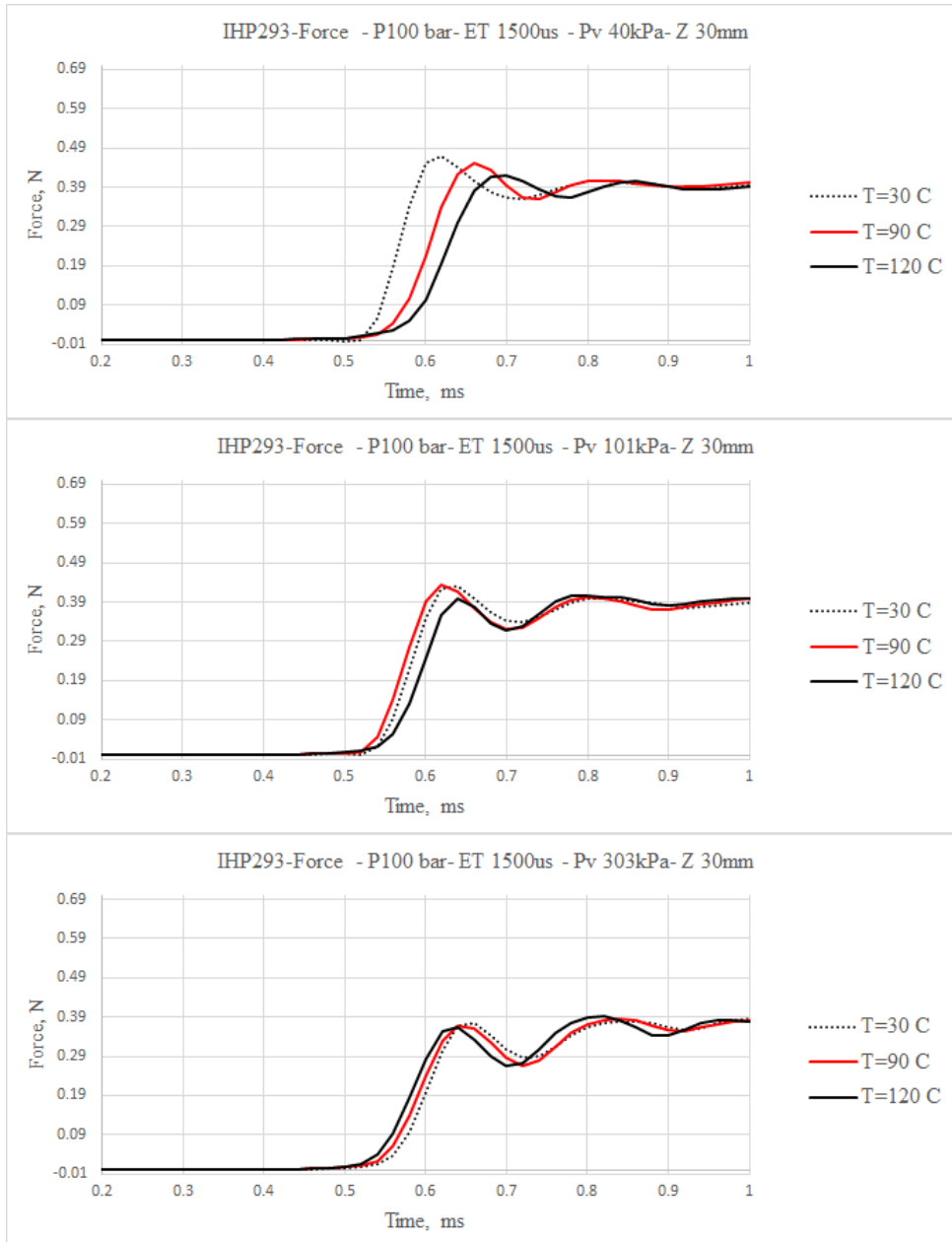


Figure 4.12. Magnified of the effect of temperature on the spray over different vessel pressure at distance Z=30 mm.

The momentum flux, integral-form results are shown in Table 4.1. As the fuel temperature increases the momentum flux decreases for the same quiescent pressure. It is reasoned by the effect of flash-boiling when it exists, otherwise, it might be the thermodynamic interactions effect that decelerates and dissipates the spray energy, see Figure 4.13. It is noteworthy to state that the value of the momentum at the operating conditions (101 KPa, 90 °C) should be less than that of the (40 Kpa, 90 °C) operating conditions in the case of non flash-boiling situation. Instead it is bigger due to the partially flash-boiling existence for the operating condition( 40 Kpa, 90 °C).

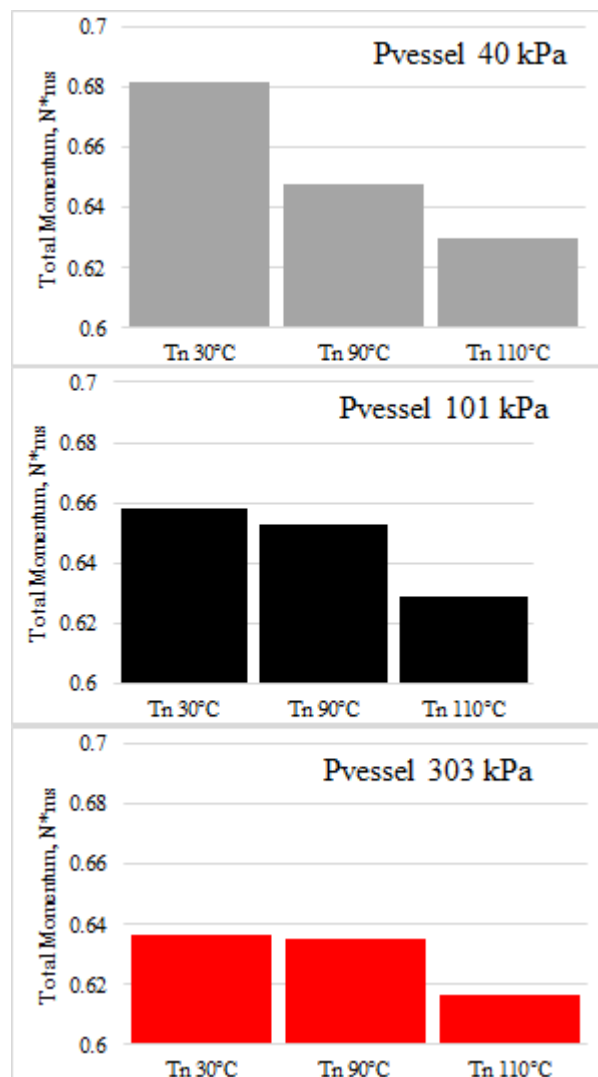


Figure 4.13. Global momentum flux-integrated measurements.

Table 4.1. Global momentum flux integral form with the related operating conditions.

Condition	$T_{nozzle} \text{ } ^\circ C$	Global
P100ET1500Tf30Ti30Pv040	30	0.68181
P100ET1500Tf30Ti30Pv0101	30	0.65828
P100ET1500Tf30Ti30Pv303	30	0.63637
P100ET1500Tf90Ti90Pv040	90	0.64749
P100ET1500Tf90Ti90Pv101	90	0.65287
P100ET1500Tf90Ti90Pv303	90	0.63544
P100ET1500Tf120Ti110Pv40	110	0.62973
P100ET1500Tf120Ti110Pv101	110	0.62886
P100ET1500Tf120Ti110Pv303	110	0.61633

#### 4.1.2. Local Momentum Test

The test was accomplished according to the prescribed test plan in the previous sections. However, preheating for the injector was achieved by injecting a couple of injections before acquiring the data at each new location, so that the repeatability concept was assured. Moreover, a number of records were acquired to achieve an unbiased test experiment. The number of points which is consisting a map and the distance between each other varied according to the spray wideness and the target-sensor distance. Furthermore, that number was chosen to be enough to make the calculation more reliable and to achieve a smooth circle integrated-map.

Figure 4.14 shows the local momentum time-integrated measurements, i.e. the integral in time of all local momentum flux values over the pre-specified map. The test was carried on over 3 fuel temperature values, 3 quiescent pressures at 10 mm distance from the nozzle and injection pressure of 100 bar.. Each operation condition is suited according to its variables; for instance at fuel temperature  $30 \text{ } ^\circ C$ , 40 KPa is located on the top-left-corner. The depicted colors resemble the value of the integrate momentum; the highest value is imitated by black color while the lowest one by dark blue. The X,Y- axes in each internal-figure in Figure 4.14 refer to the X,Y- coordinates of the sensor position with respect to the injector nozzle for each plane surface.



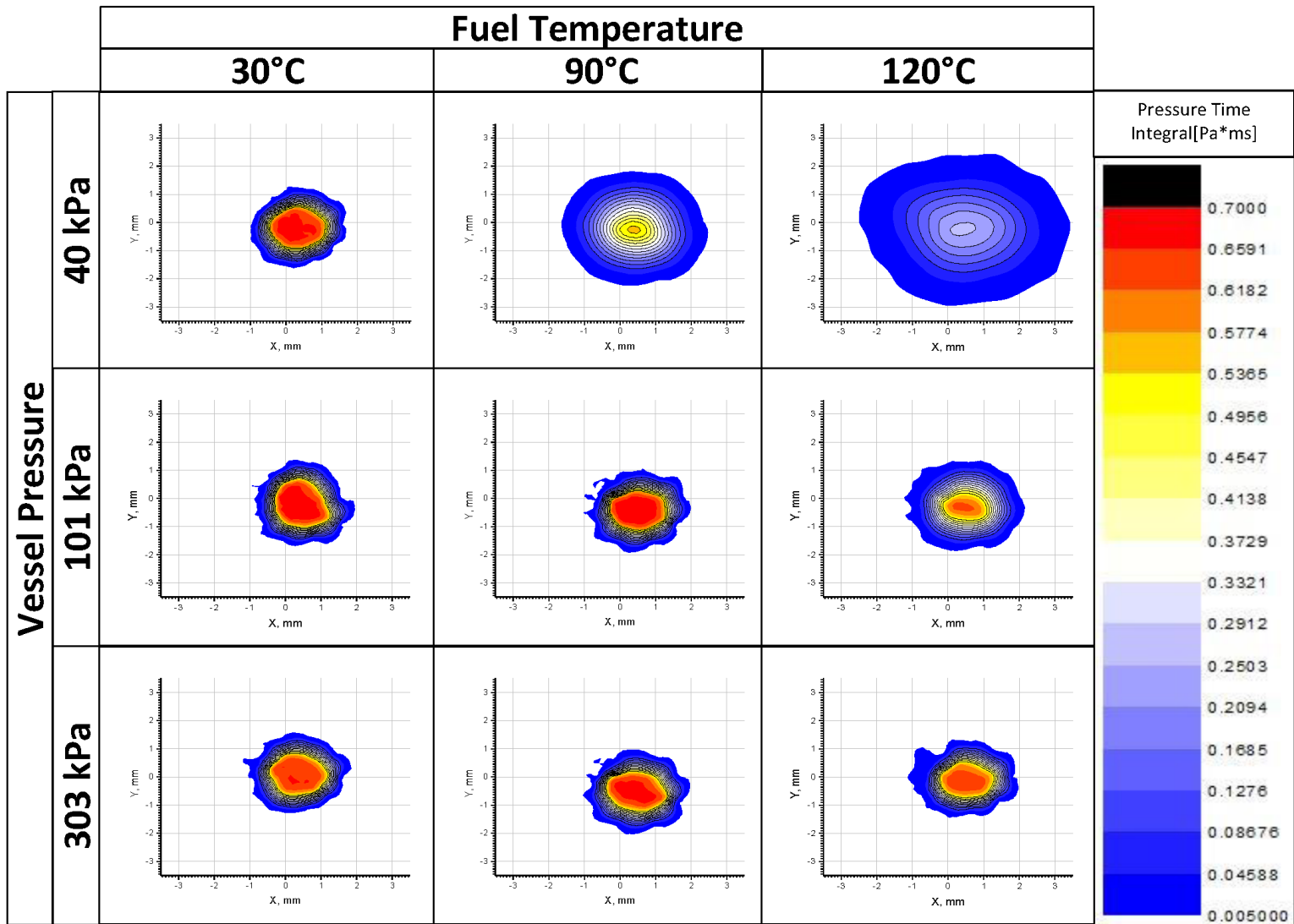


Figure 4.14. Local momentum flux results, IHP-293

The experimental condition of  $P_v$  40 KPa and  $T_f$  30 °C, which appears at the top-left-corner of Figure 4.14, occupies an area bounded by (-1 , 1.7) in X-direction and transversely in Y-direction (-1.5 , 1.2), which means that the zero-position of the the cone-hole is appreciably matching the center of spray with a deviation less than 0.5 mm in the x-axis and 0.3 mm in y-axis as well. However,  $AtSPR = 8.47$  and thus flash-boiling is not triggered.

In the second row, in the first-left figure, i.e. the experimental condition of  $T_f$  30 °C and  $P_v$  101 KPa , the detected integrated-force occupies an area bounded by (-0.8 , 1.8) in the X-axis and (-1.7 , 1.3) in the Y-axis which quite covers the same area of the ( $P_v$ 40 KPa,  $T_f$  30 °C) experimental condition. Moreover, the centralization concept among the map center and the injector nozzle was achieved with a deviation of 0.4 in the X-axis and 0.4 in the Y-axis . The figure of third row, on the first-left, i.e.  $P_v$  303 KPa and  $T_f$  30 °C experimental condition, has a similar occupied-area which is bounded by (-1 , 1.8) in the X-axis and (-1.3 , 1.5) in the Y-axis. Further, the centralization concept is quite achieved with a deviation of 0.3 in the X-axis. However, the difference in the deviation values may be attributed to the effect of vessel pressure which tilts the spray a little bit; this effect can not be triggered by means of global momentum flux technique. Generally, over the operating conditions where no flash-boiling is triggered, specifically over the left column, the effect of vessel pressure is noticed up to this end as an eccentricity of the spray perpendicular-projection of the  $P_v$  40 KPa more than that for the 101 and 303 KPa.

In the first row, in the second figure, the foot-print of the momentum is dramatically expanded; it is bounded by (-1.6 , 2.5) in the X-axis and (-2.3 , 1.8) in the Y-axis. It is noticed that its foot-print is larger than of that for  $T_f$  30 °C, for example. This belongs to the effect of flash-boiling although it is partially since the  $AtSPR$  value is less than 1 but more than 0.3. The value of the momentum is less than that for the condition  $T_f$  30 °C, for example. This result assures that the result of local momentum flux measurement in which flash-boiling appreciably decreases the value of the detected force. The second and the third ones of the second column have a similar dimension because of the flash-boiling absence with a difference in the total momentum value due to the vessel pressure.

For the third column of the Figure 4.14, the figure on the top,  $P_v$  40 KPa,  $T_f$  120 °C has the largest foot-print which extends (-2.5 , 3.5) in X-axis and (-3 , 2.3) in Y-axis. The maximum detected-force value is respectively low ( $0.33 Pa * ms$ ); due to the effect of flash-boiling in which the interaction between spray and the induced-vapor enlarges the finger-print of the detected spray as a whole. However, the force detected has the lowest value among the operation conditions tested; possibly due to the flash-boiling

phenomenon which is triggered fully-patterned with an AtSPR value of 0.22, the vapor induced in the spray makes an obstacle that hinders the spray issuing from the nozzle and disperse it.

In Figure 4.14, the figure at the third column, second row, illustrates the operation conditions of  $P_v$  101 KPa and  $T_f$  120 °C. The foot-print is larger than that of the  $P_v$  101 KPa,  $T_f$  90 °C, but is less integrated-force value due to flash-boiling partially-patterned effect.

It is noteworthy to mention that the effect of the vessel pressure on the value of the measured force is altered. As the vessel pressure increases, the value of momentum flux detected decreases correspondingly, see Figure 4.15. However, opposite to what is expected at vessel pressure 40 KPa the total momentum detected is slightly less than that for vessel pressure 101 KPa. It may be attributed to some experimental errors.

However, as it is expected, the second figure in Figure 4.15 has a momentum value descending gradually from  $P_v$  40 KPa to 303 KPa, which can be reasoned as an external force on the spray, which in turn decelerates and dissipates the spray energy. Similar to that, the third figure exhibits a similar behavior. However, a difference in the decrement percent among  $T_f$  90 and 120 °C operating conditions is obviously larger specially between  $P_v$  40 KPa and 101 KPa, which resembles the totally and partially flash-boiling condition, respectively.

### 4.1.3. Comparison Between Local and Global Momentum

The integration of the local momentum flux, theoretically should be identical to the corresponding global one. However, there is an error which can be attributed to the effect of the high temperature on the injector in addition to the nature of the local momentum appliances which exempt small slot of the spray by impinging with the edges of the cone. Table 4.2 resembles a comparison between the integrated momentum flux by means of local and global patterns. However, due to the aforementioned deficiencies a correction factor for the local momentum is applied and shown in the 5<sup>th</sup> column of Table 4.2.

In the table, it is shown that the error at the low temperature is respectively acceptable, i.e. less than 10% which is a good indication based on previous experience. However, for high temperature conditions, apart from the fully flash-boiling condition,

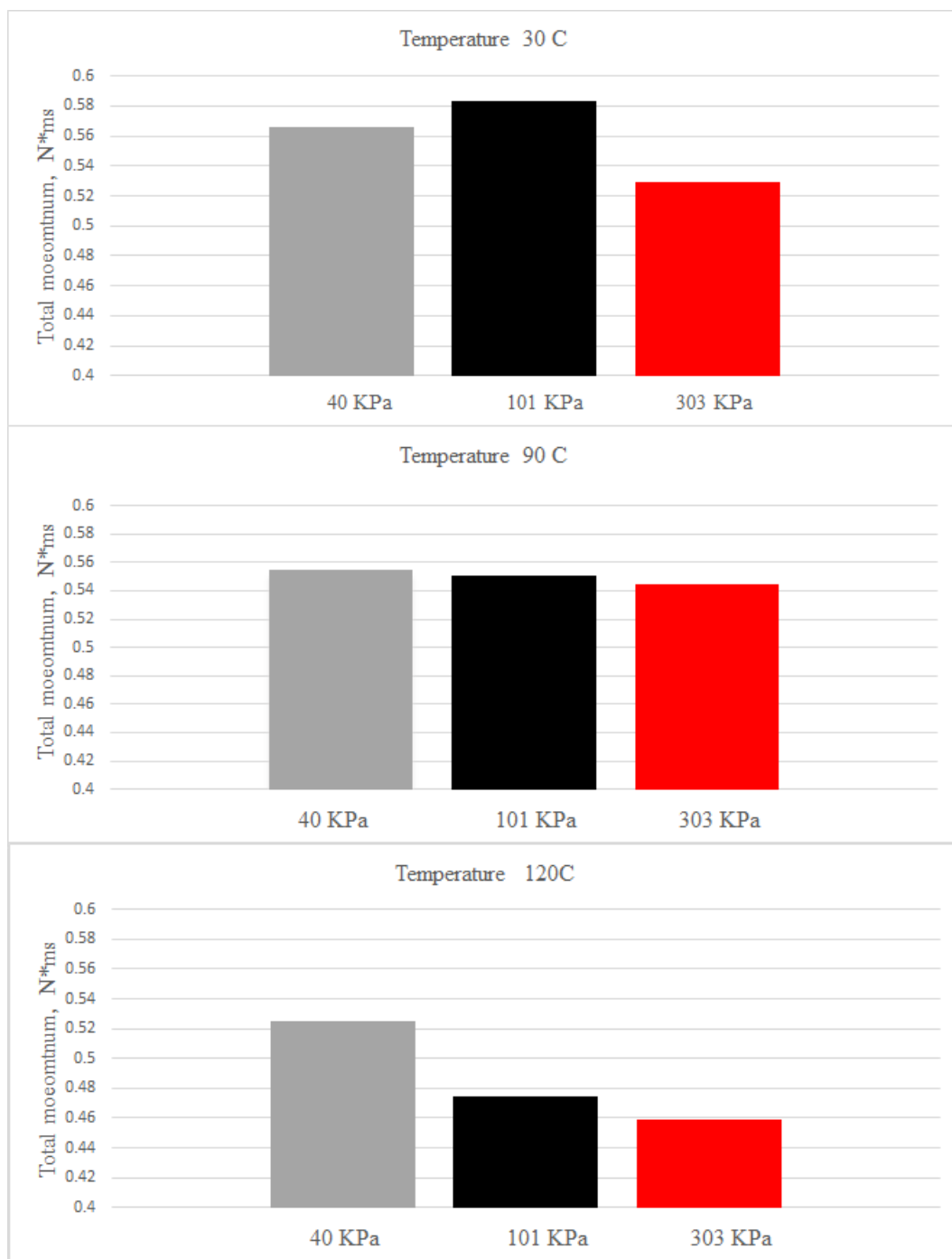


Figure 4.15. Effect of vessel pressure on the local momentum flux.

Table 4.2. Comparison between the integrated local momentum flux and the global one.

Condition	$T_n$ °C	Global	Local	Error %	Local Corr.	Err% Corr.
P100ET1500Tf30Ti30Pv040	30	0.68	0.65	4.12	0.63	7.00
P100ET1500Tf30Ti30Pv0101	30	0.66	0.67	-2.26	0.65	0.79
P100ET1500Tf30Ti30Pv303	30	0.64	0.61	4.05	0.59	6.93
P100ET1500Tf90Ti90Pv040	90	0.65	0.66	-2.02	0.62	4.09
P100ET1500Tf90Ti90Pv101	90	0.65	0.66	-0.52	0.62	5.51
P100ET1500Tf90Ti90Pv303	90	0.64	0.65	-2.07	0.61	4.05
P100ET1500Tf120Ti110Pv40	110	0.63	0.62	1.78	0.59	6.69
P100ET1500Tf120Ti110Pv101	110	0.63	0.56	11.08	0.53	15.53
P100ET1500Tf120Ti110Pv303	110	0.62	0.54	12.29	0.51	16.67

the error was significantly larger, perhaps due to the energy induced in the spray.

## 4.2. Penetration Rate

Penetration rate measurement is an essential part of the spray structure investigation; it gives an indication of how fast the spray is, and how it affects the mixing capabilities. Global momentum flux measurement itself gives an opportunity to calculate for the penetration rate by relating the time (at which the transient response starts) to the distance from the nozzle.

Figure 4.16 illustrates the effect of vessel pressure on the penetration rate over three temperature values. It is evident that vessel pressure affects the penetration rate dramatically and it is more evident at flash-boiling condition which appears at  $T_f = 120$  °C and  $P_v = 40$  KPa operating condition. However, at  $T_f = 30$  °C, the penetration rate is the highest for the lowest vessel pressure, and the penetration rate decreases when the vessel pressure increases. In the second figure, the penetration rate for the  $P_v = 101$  KPa has the maximum value, while it is less for  $P_v = 303$  KPa, and the least for  $P_v = 40$  KPa. It can be reasoned by the effect of fuel temperature which exceeds the evaporation rate and causes the flash-boiling phenomenon as well. In other words, at  $P_v = 40$  KPa a partially flash-boiling condition is achieved. Therefore, the penetration rate is the least. In the third figure, the least value of the penetration rate is seen for the fully flash-boiling condition ( $P_v = 40$  KPa). This value diverges from the others in the time of  $450 \mu s$ . However,

the value of penetration rate for  $P_v$  101 KPa seems to be less than that for  $P_v$  303 KPa, which can be attributed to the effect of flash-boiling which - in this case - seems to be stronger than the effect of the vessel pressure.

Figure 4.17 illustrates the effect of fuel temperature on the penetration rate over different vessel pressure values. In the first figure, it is noticed that the penetration rate for  $T_f = 30^\circ C$  has the maximum value while it has the least value for  $T_f = 120^\circ C$ , which can be attributed to the flash-boiling effect whether it is fully or partially.

In the second figure, the penetration rate is the lowest for  $T_f = 120^\circ C$  due to the partially flash-boiling phenomenon. However, the penetration rate for  $T_f = 90^\circ C$  is higher than that for  $T_f = 30^\circ C$  although there is no flash-boiling triggered, which is perhaps due to the high temperature and its corresponding molecular interaction.

In the third figure, the three penetration rates are more compact to each other up to time = 550  $\mu s$ . However, the penetration rate corresponding to  $T_f = 30^\circ C$  is delayed a little bit, while both at  $T_f = 90, 120^\circ C$  are almost identical through over the operation. It may be attributed to the vapor content and its energy which supports the spray to penetrate more.

It is worth to mention that penetration rate can be easily measured by means of high-speed imaging, providing that the effect of vapor content is not included. However, the power of momentum flux in predicting the penetration rate comes from the fact that it takes into account the vapor involved. A comparison with a precedent work of measuring the penetration rate utilizing the high-speed imaging technique is shown in Figure 4.18, in which the x-axis represents the time in  $\mu s$ , and the y-axis represents the penetration rate in mm units. It is noteworthy to mention that as the temperature increases the penetration rate increases correspondingly at vacuum vessel pressure condition. Further, at fully flash-boiling phenomenon, the vapor affects the penetration rate apparently and makes it the shortest one among the different temperatures under  $P_v$  40 KPa. At  $P_v$  100 Kpa the penetration rate is shorter than that for  $P_v$  303 Kpa but it is slightly longer than that for  $P_v$  40 Kpa due to the vapor induced in the spray because of the flash-boiling.

When the fuel temperature is high, the penetration rate is low in a specific range 80 - 120  $^\circ C$ . However in the temperature range of 20 - 60  $^\circ C$ , no changes were experienced as stated in (Bosi, 2014), which is consistent with the results of the common ranges.

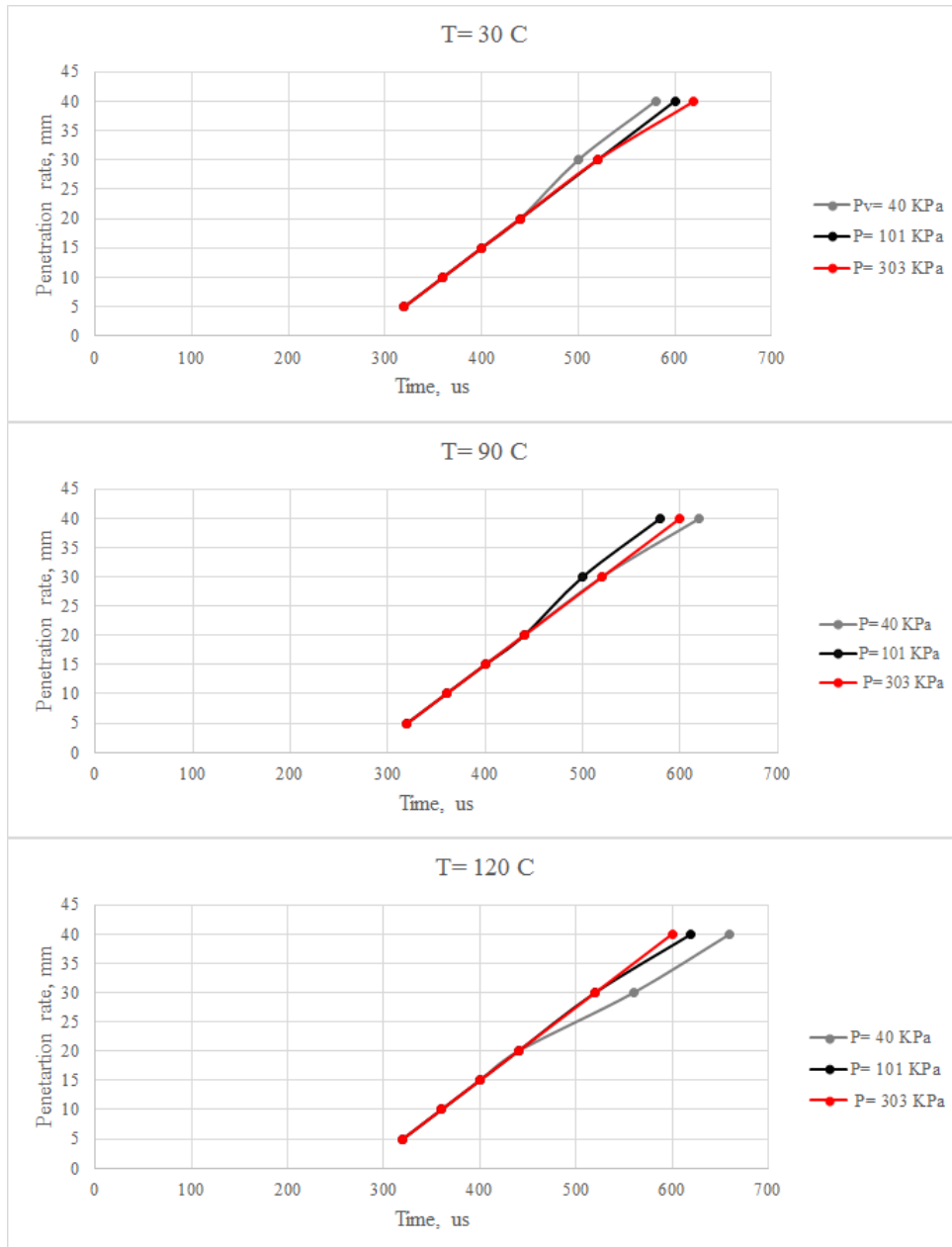


Figure 4.16. Effect of vessel pressure on the penetration rate.

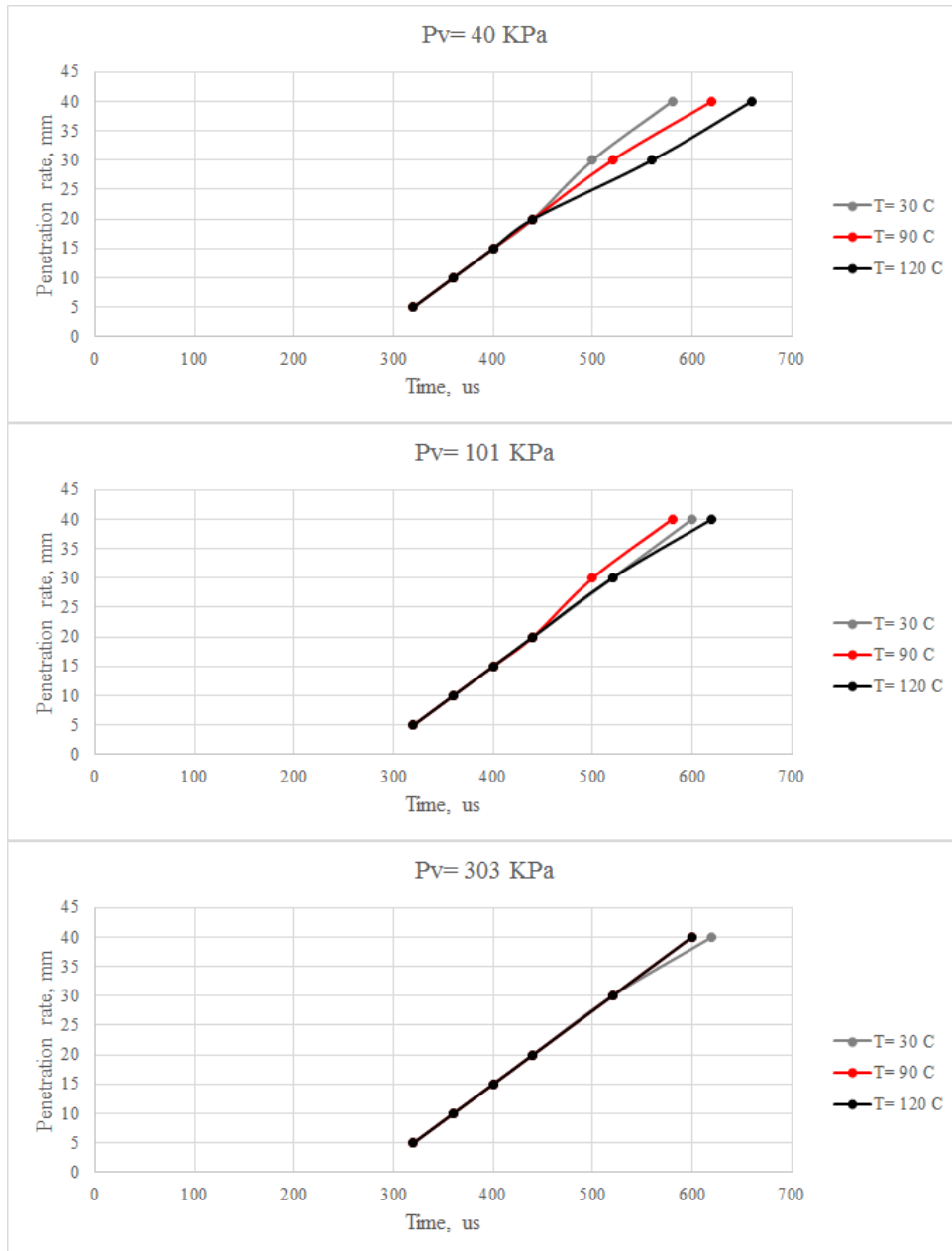


Figure 4.17. Effect of fuel temperature on the penetration rate.



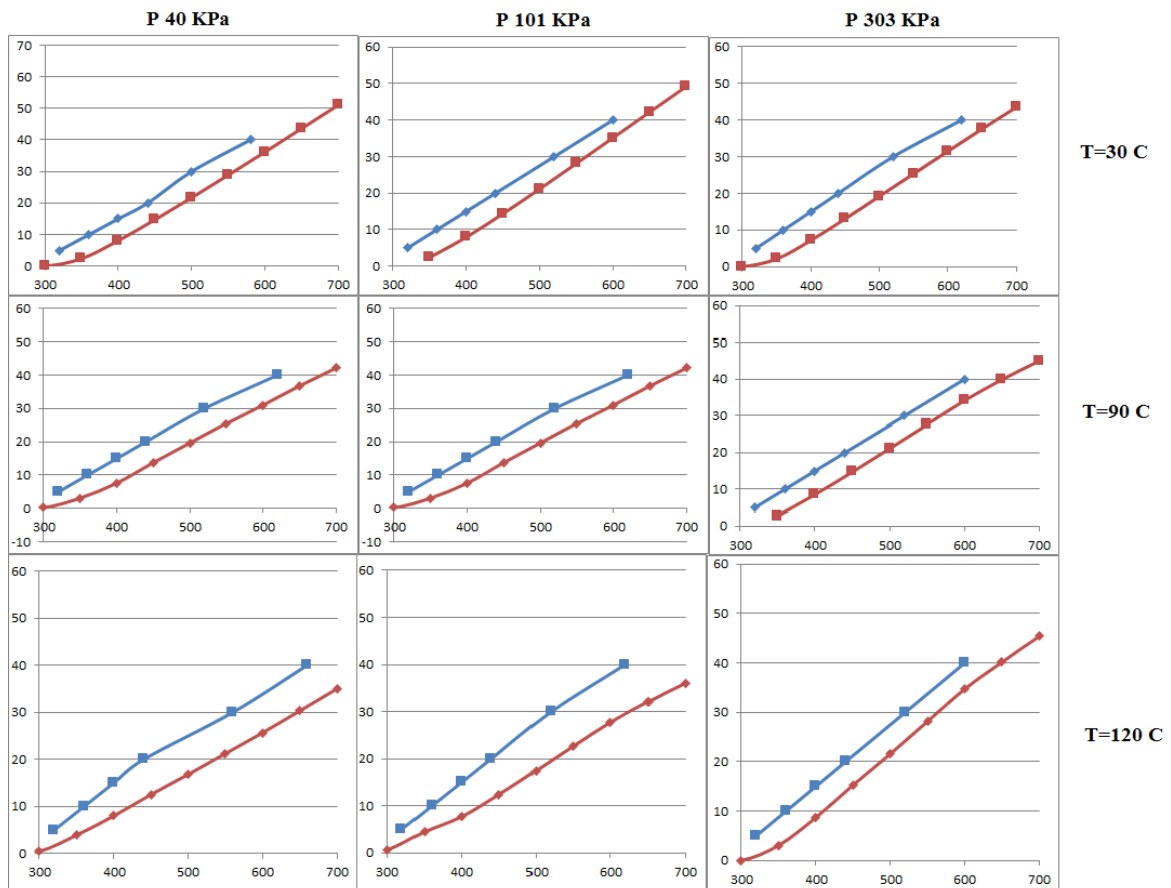


Figure 4.18. Comparison of penetration rate measured from momentum VS imaging; blue refers to momentum, and dark red refers to high-speed imaging, imaging results are integrated from (Bosi, 2014).

### 4.3. Spray Cone Angle

As a complementary of spray structure investigation, high-speed imaging technique facilitates measuring the so-called spray cone angle which defines the angle between the spray borders. Further spray cone angle can be detected by means of spatial momentum flux; via applying the Pythagorean concept on the little triangle-shape which has the triangle-base as the distance from the nozzle and the horizontal segment as the mean radius of the circle-shape local momentum flux map (Figure 4.19). It is noteworthy to mention that the participation of the vapor content induced in the spray is triggered by the local momentum flux. However, in the high-speed imaging which the visible part of the spray in the post-process stage is only considered in the cone angle calculation.

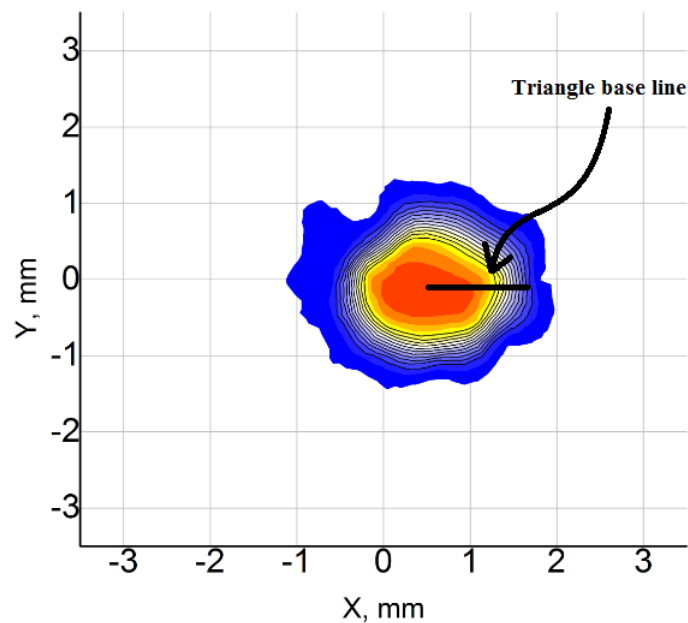


Figure 4.19. Cone angle measurement concept utilizing local momentum flux.

In Figure 4.19, cone angle calculation depends on the distance of the map from the injector tip. However, utilizing high-speed imaging technique dictates capturing photos at different time-frames. Then, post-processing via special software to calculate for the time-history of cone angle.

Figure 4.20 elucidates images for different operating conditions in which the cone angle appears quite clearly, integrated from (Postrioti et al., 2015). The up-right-corner figure has the widest, shortest cone angle due to flash-boiling effect, which was assured by means of spatial momentum flux results. Furthermore, it has the shortest penetration rate

due to the same reason, which was triggered utilizing the results of global momentum flux. However, there is a good agreement among the high-speed imaging results with those of the momentum flux in terms of cone angle and penetration rate as well.

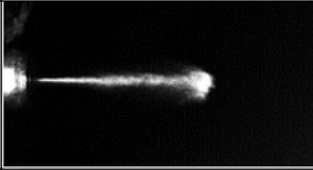
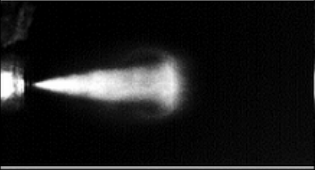
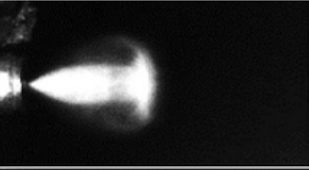
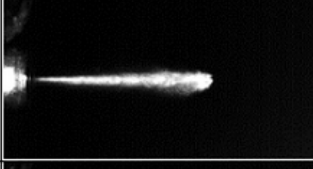

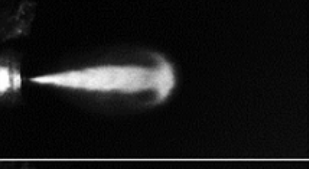
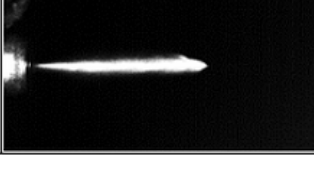
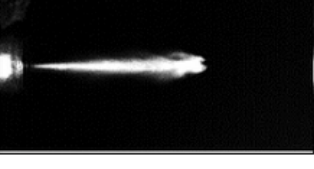
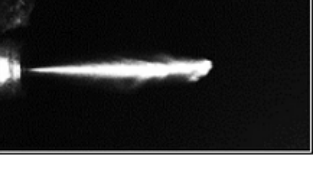
Test Vessel Pressure	Injector Nozzle & Fuel Temperature		
	30 °C	90 °C	120 °C
40 kPa			
101 kPa			
303 kPa			

Figure 4.20. High speed imaging for different experimental conditions for IHP-293 injector.

Source: (Postrioti et al., 2015)

## CHAPTER 5

### CONCLUSION

In this study, two research single-hole injectors were tested to figure out spray structure under flash-boiling and non flash-boiling conditions. A great attention was paid for the IHP-293 research injector (due to its L/D value) in terms of momentum flux measurements, the integrated-results of high-speed imaging for both penetration rate and cone angle as well. Over three fuel-temperature values (30, 90, 120 °C), three vessel pressures (40, 101, 303 KPa), two energizing times (1.5, 3 ms) tests were carried out and the main conclusions can be summarized as follows:

In the high-speed imaging, flash-boiling phenomenon apparently affects spray shape comparing to its shape in standard conditions and spray looks less compact due to the vapor content inside its structure; shorter penetration rate with wider cone angle which can improve evaporation rate and consequently mixing capabilities.

In the fully flash-boiling condition the penetration rate is dramatically decreased; i.e. at AtSPR less than 0.3, for example  $P_v$  40 KPa,  $T_f$  120 °C, penetration rate is approximately 40% of that at 30 °C for the same vessel pressure. Furthermore, a significant enlargement in the cone angle from 4 to 17 degrees amongst 30 °C, for example.

In the transition period (0.3 AtSPR < 1.0), spray structure has apparently been altered in terms of penetration-rate reduction and cone-angle widening, as can be noticed at  $T_f=90$  °C and  $P_v=101$  KPa, which can assist mixing potentials and inject less fuel in that conditions.

For the non flash-boiling condition, spray structure seems to be more compact with a relatively small cone angle, such as 4° for a vacuum and low temperature experimental condition, which permits more penetration and less evaporation rate as well.

The flash-boiling onset does not affect the momentum flux measurements.

In the high temperature condition, the injector experienced a reduction in the injection duration, which may be attributed to the electro-mechanical components rather than fluid dynamic effects.

In the local momentum flux measurements, at flash-boiling effect the fingerprint experienced a significant enlargement with a corresponding less in the local momentum

peak intensity, which can be triggered by means of high-speed imaging results. However, it refers to an increase in the cone angle that leads to an improvement in the air/fuel mixing abilities.

There is a good agreement among the integration of the local momentum measurements and the global ones, however the error for the low-temperature is below 8% whereas for high temperatures it is around 15%, which may be attributed to the loss in the measured spray.

Flash-boiling happens when fuel is injected into the chamber under an ambient pressure less than the saturation pressure of the fuel at the same temperature. Furthermore, this phenomenon is beneficial for its atomization improvement. This study enhances the understanding of flash-boiling in addition to its factors and consequently extends the range at which flash-boiling occurs in the possible operating conditions. As an example of this extension, heating up the fuel under the same chamber pressure extends the range of flash-boiling occurrence.

In the anticipated future an improvement in the air/fuel mixing capabilities can be achieved by means of heating up the injected fuel and the injector nozzle-tip as well, under a well-defined mass flow rate.

## REFERENCES

- Bosi, M. (2013-2014). *Analisi sperimentale di iniettori Gasoline Direct Injection in condizioni di flash boiling*. Ph. D. thesis, UNIVERSITA' DEGLI STUDI DI PERUGIA.
- Carsten, B. (2006). Modern concepts. *Mixture Formation in Internal Combustion Engine*, 225–286.
- Chigier, N. and R. D. Reitz (1996). Regimes of jet breakup and breakup mechanisms-physical aspects. *Recent advances in spray combustion: Spray atomization and drop burning phenomena. 1*, 109–135.
- Dan, T., T. Yamamoto, J. Senda, and H. Fujimoto (1997). Effect of nozzle configurations for characteristics of non-reacting diesel fuel spray. Technical report, SAE Technical Paper. 970355.
- Desantes, J., R. Payri, F. Salvador, and J. Gimeno (2003). Measurements of spray momentum for the study of cavitation in diesel injection nozzles. Technical report, SAE Technical Paper. 01-0703.
- Desantes, J. M., R. Payri, F. J. Salvador, and J. Gimeno (2006). Prediction of spray penetration by means of spray momentum flux. Technical report, SAE Technical Paper. 01-1387.
- Iwamoto, Y., K. Noma, O. Nakayama, T. Yamauchi, and H. Ando (1997). Development of gasoline direct injection engine. Technical report, SAE Technical Paper. 970541.
- Leroux, S., C. Dumouchel, and M. Ledoux (1996). The stability curve of newtonian liquid jets. *Atomization and Sprays*.
- Lin, S. and R. Reitz (1998). Drop and spray formation from a liquid jet. *Annual Review of Fluid Mechanics* 30(1), 85–105.
- Michael, P., G. Giovanni, R. Rossella, and A. Demaio (2005). Reduction of spray momentum for gdi high-pressure injectors-a necessary step to accomplish series production of super-charged di-engines. Technical report, SAE Technical Paper. 01-0104.
- Miesse, C. (1955). Correlation of experimental data on the disintegration of liquid jets. *Industrial & Engineering Chemistry* 47(9), 1690–1701.
- Nurick, W. (1976). Orifice cavitation and its effect on spray mixing. *Journal of fluids engineering* 98(4), 681–687.
- Payri, R., J. Garcia, F. Salvador, and J. Gimeno (2005). Using spray momentum flux measurements to understand the influence of diesel nozzle geometry on spray characteristics. *Fuel* 84(5), 551–561.
- Postrioti, L. and M. Battistoni (2010). Evaluation of diesel spray momentum flux in tran-

- sient flow conditions. Technical report, SAE Technical Paper. 1-2244.
- Postrioti, L., M. Battistoni, C. Ungaro, and A. Mariani (2011). Analysis of diesel spray momentum flux spatial distribution. Technical report, SAE Technical Paper. 01-0682.
- Postrioti, L., M. Bosi, R. Di Gioia, and B. G (2015). Gdi spray evolution and sizing characteristics in flash-boiling conditions. Technical report, SAE Technical Paper.
- Postrioti, L., M. Bosi, A. Mariani, and C. Ungaro (2012). Momentum flux spatial distribution and pda analysis of a gdi spray. Technical report, SAE Technical Paper. 01-0459.
- Postrioti, L., F. Mariani, M. Battistoni, and A. Mariani (2009). Experimental and numerical evaluation of diesel spray momentum flux. Technical report, SAE Technical Paper. 01-2772.
- Ranz, W. E. (1956). *On sprays and spraying*. Dep. Eng. Res. Penn. State Univ. Bull 65.
- RD, R. and B. FV (1986). *Encyclopedia of Fluid Mechanics*, Chapter Mechanisms of Breakup of Round Liquid Jets. Gulf Publishing, Huston, Texas.
- Reitz, R. and F. Bracco (1982). Mechanism of atomization of a liquid jet. *Physics of Fluids (1958-1988)* 25(10), 1730–1742.
- Reitz, R. D. (1987). Modeling atomization processes in high-pressure vaporizing sprays. *Atomisation Spray Technology* 3, 309–337.
- Schwarz, C., E. Schnemann, B. Durst, J. Fischer, and A. Witt (2006). Potential of the spray- guided bmw di combustion system. *SAE Technical Paper. 01-1265*.
- Sterling, A. M. and C. Sleicher (1975). The instability of capillary jets. *Journal of Fluid Mechanics* 68(03), 477–495.
- Taylor, G. (1940). Generation of ripples by wind blowing over a viscous fluid. *The Scientific Papers of GI Taylor* 3, 244–254.
- Xu, M., Y. Zhang, W. Zeng, G. Zhang, and M. Zhang (2013). Flash boiling: easy and better way to generate ideal sprays than the high injection pressure. Technical report, SAE Technical Paper. 01-1614.
- Zhao, H. (2010). *Advanced direct injection combustion engine technologies and development*, Volume Gasoline and gas engines, Chapter Overview of gasoline direct injection engines. Woodhead Publishing Limited.